







# The Star Formation Across Cosmic Time (SFACT) Survey. II. The First Catalog from a New Narrowband Survey for Emission-line Objects

Jennifer Sieben<sup>1,3</sup> , David J. Carr<sup>1</sup> , John J. Salzer<sup>1</sup> , and Alec S. Hirschauer<sup>1,2</sup> <sup>1</sup> Indiana University, 727 East 3rd Street, Bloomington, IN 47405, USA<sup>2</sup> Space Telescope Science Institute, 3700 San Martin Drive, Baltimore, MD 21218, USA; [jsieben@iu.edu](mailto:jsieben@iu.edu)

Received 2022 June 3; revised 2023 June 30; accepted 2023 July 9; published 2023 August 11

## Abstract

Star Formation Across Cosmic Time (SFACT) is a new narrowband (NB) survey designed to detect faint emission-line galaxies (ELGs) and QSOs over a broad range of redshifts. Here we present the first list of SFACT candidates from our pilot-study fields. Using the WIYN 3.5 m telescope, we are able to achieve good image quality with excellent depth and routinely detect ELGs to  $r=25.0$ . The limiting line flux of the survey is  $\sim 1.0 \times 10^{-16} \text{ erg s}^{-1} \text{ cm}^{-2}$ . SFACT targets three primary emission lines:  $\text{H}\alpha$ ,  $[\text{O III}] \lambda 5007$ , and  $[\text{O II}] \lambda 3727$ . The corresponding redshift windows allow for the detection of objects at  $z \sim 0-1$ . With a coverage of  $1.50 \text{ deg}^2$  in our three pilot-study fields, a total of 533 SFACT candidates have been detected (355 candidates  $\text{deg}^{-2}$ ). We detail the process by which these candidates are selected in an efficient and primarily automated manner, then tabulate accurate coordinates, broadband photometry, and NB fluxes for each source.

*Unified Astronomy Thesaurus concepts:* Galaxy evolution (594); Emission line galaxies (459); Starburst galaxies (1570); Surveys (1671); Star formation (1569); Galaxy Abundances (574); Spiral galaxies (1560); Blue compact dwarf galaxies (165); Seyfert galaxies (1447); Dwarf galaxies (416); Quasars (1319)

*Supporting material:* machine-readable tables

## 1. Introduction

The Star Formation Across Cosmic Time (SFACT) survey is an ongoing wide-field imaging and spectroscopic program which targets the detection of large numbers of extragalactic emission-line sources. As a narrowband (NB) survey, SFACT is able to discover a wealth of new sources exhibiting strong emission lines. The SFACT survey methodology draws upon the rich legacy of previous emission-line galaxy (ELG) surveys (e.g., MacAlpine et al. 1977; Boroson et al. 1983; Markarian & Stepanian 1983; Salzer et al. 2000, 2020; Ryan-Weber et al. 2004; Kakazu et al. 2007; Werk et al. 2010; Ly et al. 2011; Kellar et al. 2012; Sobral et al. 2012, 2013; Stroe & Sobral 2015; Cook et al. 2019; Khostovan et al. 2020; Watkins et al. 2021; Martínez-Solaache et al. 2022). SFACT builds on this previous work, using a medium-class telescope with a wide field of view (FOV) and three custom NB filters.

The goal of the SFACT survey is to produce a high-quality catalog of emission-line objects whose selection function and completeness limits can be accurately quantified, so that the resulting catalog of ELGs will be useful for a broad range of studies requiring statistically complete galaxy samples. A comprehensive description of the survey is given in Salzer et al. (2023, henceforth referred to as SFACT1). SFACT is designed to both cover a wide area on the sky and to be deep. When completed, the total area covered by the survey will be between 25 and 30  $\text{deg}^2$ . Furthermore, our data routinely reach a

limiting line flux detection level of  $\sim 1.0 \times 10^{-16} \text{ erg s}^{-1} \text{ cm}^{-2}$ . These survey parameters represent compromises. SFACT does not reach the ultra-faint flux levels of extremely deep NB surveys (e.g., Sobral et al. 2012, 2013; Khostovan et al. 2020), but it does cover much larger survey areas. Conversely, SFACT does not have the extreme FOV coverage of surveys like Cook et al. (2019) and Martínez-Solaache et al. (2022), but it reaches to substantially deeper detection limits.

The current paper is one of a series of three initial SFACT publications that present survey results for our pilot-study fields. SFACT1 presents the survey description, goals, and motivation. It also provides a summary of the properties of the 533 ELGs detected in our first three survey fields (magnitudes, luminosities, redshifts, line fluxes, star formation rates, etc.). Example objects are shown that illustrate the types of objects being detected by SFACT; both imaging and spectroscopic data are presented. SFACT1 also explores numerous science applications that can be addressed with the full survey. The current paper (SFACT2) presents the initial survey lists selected from the imaging portion of the survey. We provide details of our observing and image-processing procedures as well as how the ELGs are selected. We illustrate our survey method with numerous examples of sources discovered in our NB images, and summarize the properties of the sample derived from our imaging data. The third SFACT paper (Carr et al. 2023, henceforth referred to as SFACT3) focuses on the spectroscopic component of the survey, discussing the procedures for the observations and processing of the spectral data. SFACT3 tabulates key spectroscopic data obtained for the ELGs in our pilot-study fields. These data are used to verify the nature of the objects discovered in the imaging data and to derive a range of key parameters. SFACT3 also presents the spectra corresponding to the example images shown in SFACT2.

<sup>3</sup> Visiting astronomer, Kitt Peak National Observatory at NSF's NOIRLab, which is managed by the Association of Universities for Research in Astronomy (AURA) under a cooperative agreement with the National Science Foundation.



**Table 1**  
Observation Dates

Field	Filter	Observation Date	FWHM PSF	$\alpha$ (J2000)	$\delta$ (J2000)
SFF01	<i>r</i>	09/17/2017	0"89	21:42:42	19:59:28
	<i>i</i>	09/17/2017	0"83		
	<i>g</i>	09/17/2017	0"76		
	NB1	09/13/2018	0"93		
	NB2	09/14/2018	0"78		
	NB3	09/13/2018	0"96		
SFF10	<i>r</i>	11/07/2016	0"83	01:44:20	27:54:13
	<i>i</i>	08/19/2017	0"81		
	<i>g</i>	08/19/2017	1"23		
	NB1	11/07/2016	0"85		
	NB2	09/14/2018	0"85		
	NB3	09/13/2018	0"69		
SFF15	<i>r</i>	11/07/2016	0"81	02:38:52	27:51:43
	<i>i</i>	08/19/2017	0"87		
	<i>g</i>	08/19/2017	1"17		
	NB1	11/07/2016	0"72		
	NB2	09/14/2018	0"70		
	NB3	09/14/2018	0"66		

In this paper, we first describe our observational procedures (Section 2.1) and our data-processing technique (Section 2.2). Our method for selecting objects for inclusion in our survey catalogs is detailed in Section 3, along with our photometry method and calibration in Section 3.3. The results of the pilot study, including the data and example objects, are presented in Section 4. For all of the SFACT papers, we assume a standard Lambda cold dark matter ( $\Lambda$ CDM) cosmology with  $\Omega_m = 0.27$ ,  $\Omega_\Lambda = 0.73$ , and  $H_0 = 70 \text{ km s}^{-1} \text{ Mpc}^{-1}$ .

## 2. Observations and Data Processing

### 2.1. Observations

All survey imaging data were acquired using the One Degree Imager (ODI; Harbeck et al. 2010) on the WIYN<sup>4</sup> 3.5 m telescope sited at Kitt Peak, Arizona. ODI consists of 30 orthogonal transfer array (OTA) CCDs, each of which comprises  $64 \times 480 \times 496$  pixel cells. The pixel size for the ODI OTAs is  $12\mu$ , which yields an image scale of  $0''.11 \text{ pixel}^{-1}$ . The total FOV of ODI is  $40' \times 48'$ . All survey fields are observed through six filters: three BB filters (*gri*) and three NB filters. The BB data were obtained through *g*, *r*, and *i* filters  $\sim 1500 \text{ \AA}$  in width. The BB bandpasses mimic the Sloan Digital Sky Survey (SDSS) filters (York et al. 2000).

The fields observed for SFACT were selected to overlap with the SDSS (York et al. 2000; Aguado et al. 2019), which we used for photometric calibrations. Two of the fields presented in this pilot study were centered on ELGs found in the previous  $H\alpha$  Dots survey (Kellar et al. 2012; Salzer et al. 2020; Watkins et al. 2021). This provided a valuable test bed for the current survey methodology. The selection of the SFACT survey fields is discussed in more detail in SFACT1.

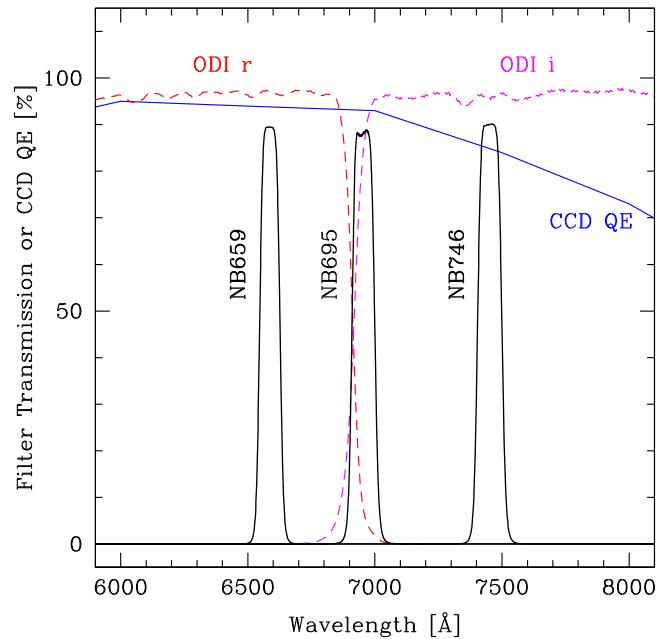


**Figure 1.** The filter transmission curves of our three narrowband filters: NB659 (NB2), NB695 (NB1), and NB746 (NB3). The dashed lines show part of the transmission curves for the *r* and *i* broadband filters. Overlaid is the quantum efficiency (QE) curve of the CCD (solid line), demonstrating that while it does start to drop off around  $7000 \text{ \AA}$ , the sensitivity is still high in *i* and NB3.

#### 2.1.1. Science Observations

The imaging data used for this paper were obtained during three observing seasons. For a full list of observing dates, see Table 1. In 2016 November, initial test data were acquired for the SFF10 and SFF15 fields in the *r* band and first narrowband filter (NB1). These observations provided the data used to develop our processing and object-selection methods (see Section 3). In 2017, we added additional broadband (BB) observations of SFF10 and SFF15 in the *g* and *i* bands plus included an additional field (SFF01). Our data set for the pilot study was then completed upon the subsequent addition of two additional NB filters in 2018.

The NB data were obtained through three special filters designed for the survey, centered at  $6590$ ,  $6950$ , and  $7460 \text{ \AA}$ , each with a width of  $\sim 90 \text{ \AA}$  (henceforth NB2, NB1, and NB3, respectively). The exact bandpasses are detailed in SFACT1 as well as the redshift ranges accessible via commonly detected emission lines. The transmission curves of our NB filters are shown in Figure 1. The three NB filters fall within the *r* or *i* BB filters and are in a region where the CCD sensitivity is quite high.

All NB and BB images were taken using a nine-point dither pattern. The dither sequence is a carefully planned sequence of position adjustments in order to move sources off of bad columns, chip gaps, or dead OTA cells on the camera. By moving the telescope such that inactive areas on the camera are not always covering the same region on the sky, we ensured that we were truly covering the full available FOV. In this way, multiple exposures of the same fields increased image depth, allowing for the detection of fainter sources.

Each individual NB exposure was  $600 \text{ s}$ , for a total integration time of  $90 \text{ minutes}$  for each NB dither sequence. Because each pixel in the final stacked images is typically illuminated by the sky in only 6–7 images in the dither

<sup>4</sup> The WIYN Observatory is a joint facility of the University of Wisconsin-Madison, Indiana University, NSF's NOIRLab, the Pennsylvania State University, and Purdue University.

sequence, the effective exposure time is closer to 60–70 minutes for each pixel in the NB images. Each individual BB exposure was 120 s, and the final stacked BB images likewise include light from 6–7 images in a given pixel of the final stacked image.

When using ODI, telescope tracking occurs using a star located on one of the OTA chips, which is read out continuously during the exposure at video rates. Because the OTA chip used for guiding is lost to the science image, we attempted to select guide stars located on different OTAs for each image in the dither sequence. This avoids large unusable areas in our final stacked images.

### 2.1.2. Calibration Observations

Following standard observing procedures, bias and dark images were taken each night. This included 10 zero-second bias frames followed by three 600 s dark current images. These are crucial for correcting detector signatures during the initial processing. Spectrophotometric standard star observations were also taken; these are further discussed in Section 3.3.1.

Flat-field images are taken by the WIYN staff approximately once per month through each filter and are applied to the processing of the recently taken data. A special technique is employed. A slow shutter blade speed is used in order to baffle out internal reflections, and thus eliminate the pupil ghost. The slow shutter technique works such that both shutters move at once, with only a small delay between them, effectively creating a slit aperture which moves across the frame. Raw flat-field images are acquired with at least two different rotations of the instrument so that any gradients because of nonuniform illumination of the flat field can be smoothed out. The stability of the flats is very good, with variations of less than 1% over many months.

## 2.2. Data Processing

Raw images are processed and analyzed utilizing both the ODI Pipeline, Portal, and Archive (PPA), as well as custom scripts written in IRAF and Python. Each of the processing steps are detailed in the following subsections.

### 2.2.1. ODI Pipeline, Portal, and Archive

Raw ODI images are transferred from WIYN to the PPA, which is hosted by Indiana University. In the PPA, the raw data are first run through the QuickReduce pipeline (Kotulla 2014), which begins by masking out unusable pixels, whether this is due to persistency, trailing, a defective cell, cross talk, or a static bad pixel. Overscan levels, bias, and dark levels are determined and subtracted from each of the raw images. A correction based on the flat fields and any known nonlinearity between the observed counts and the exposure is then applied. The final step is an astrometric calibration, which is performed using Gaia (Gaia Collaboration et al. 2016a, 2016b) as the reference catalog. The output from QuickReduce is one complete FITS image for each dither position, properly reduced and ready for further processing.

Next, the astrometric mapping software SWarp (Bertin et al. 2002) is run from within the PPA, which aligns and combines all of our images from each dither sequence to produce one image for each filter for each field. We use a weighted combination mode, an illumination correction, and utilize a surface fit for the background-subtraction method, preserving

extended objects of at least  $3'$ . The process also masks bad pixels and removes the OTAs used in guiding. The output image is reprojected with a new pixel scale of  $0''.125 \text{ pixel}^{-1}$ .

### 2.2.2. SFACT Preprocessing Steps

The reduced and stacked ODI images are retrieved from the PPA for subsequent processing. The image from each filter is cropped such that all images for each field cover exactly the same area on the sky and are precisely aligned with one another. This ensures that the objects identified in a field have the same positions in each filter later in the processing.

A master image is then created by summing all six individual images together, resulting in a very deep image. Objects as faint as  $r \sim 26$  are readily detected in the master image. This deep master image is used for catalog creation, as discussed in Section 3. Because this image includes both NB and BB filters, it allows for the detection of ELGs that have extremely faint continuum flux but strong nebular emission, which would otherwise be missed in a BB-only image.

The average point-spread function (PSF) FWHM is determined using roughly a dozen user-selected stars. This measure of the image quality is determined for the master image as well as the individual filter images. All images are then binned  $2 \times 2$ , resulting in a final image scale of  $0''.25 \text{ pixel}^{-1}$ . This value was chosen because a native resolution (seeing) better than  $0''.5 \text{ pixel}^{-1}$  is only rarely obtained at WIYN. While our objects tend to have small angular sizes, they are almost never undersampled with this choice of pixel scale. Finally, a script is run on the binned master image, which allows the user to select an object-free region in order to determine the background noise level, a crucial parameter used during the object-detection stage.

The final step in the preprocessing of the images is to create scaled *continuum images* appropriate for each NB image. These scaled images, which are derived from our survey BB images, are used as part of our object-selection process (described in Section 3), as well as for creating continuum-free difference images (as illustrated in Section 4.2).

As seen in Figure 1, the NB1 filter is located at the transition between the  $r$ -band and  $i$ -band filters, while NB2 is located in the redder half of the  $r$ -band filter. As a result of these locations, extremely red objects (e.g., M stars and high-redshift, early-type galaxies) show a significant flux excess in both NB1 and NB2 when only the  $r$ -filter image is used as the continuum image, leading to false detections. Tests revealed that the sum of the  $r$ - and  $i$ -filter images provides far better results as the continuum images for both NB1 and NB2 than does using the  $r$ -band image alone. On the other hand, the  $i$ -band image proves adequate for use as the continuum image for NB3.

As a result of our evaluation, we adopt the sum of the  $r$ -band and  $i$ -band images ( $r + i$ ) as the continuum image for the NB1 and NB2 images and the  $i$ -band image as the continuum image for NB3. All three continuum images are then scaled to match the flux levels in the individual NB filter images. This is done by measuring the fluxes of approximately a dozen user-selected stars in both the continuum and NB images and then scaling the continuum image to match the flux in the NB image. These scale factors account for numerous factors, such as the differences in filter bandwidths, exposure times, air mass, and sky transparency. The first two terms always dominate, meaning that the scale factors derived this way have characteristic values that reflect the ratios of the filter



bandwidths and exposure times. For example, the ratio of the bandwidths of the  $r+i$  and NB1 filters is  $\sim 28.6$ , while the ratio of the exposure times is 0.2. This results in an expected scale factor of  $\sim 5.7$ , which is the middle of the range of measured scale factors we determine. Similarly, the scale factors for the NB2 and NB3 continuum images have characteristic values of  $\sim 6.4$  and  $\sim 2.7$ .

### 3. SFACT Object Selection and Photometry

In the following section, we detail the methods carried out to select and measure emission-line candidates from our survey images. The first step utilizes the ultra-deep master image of each field to create a comprehensive catalog of all objects detected within this image. Next, we perform small-aperture photometry on every object in the catalog using the continuum and NB images and identify those sources that exhibit an excess of flux in the NB image, indicating a potential ELG or QSO. All candidates are then checked visually to remove objects that are image artifacts. Once the final list of SFACT candidates is established, each source in the final catalog of ELGs is carefully measured in all three BB images ( $gri$ ) as well as the relevant NB image.

Each survey field typically contains on the order of  $10^5$  total objects detected at the sensitivity limit of our master image. Custom scripts were written to identify relevant objects in a fully automated process. These scripts were implemented to reduce the large number of objects that needed to be evaluated as possible ELG candidates in each field to a manageable level. Manual verification was performed as a last step. We perform the following analysis on quadrants (designated A–D) of our full-frame images in order to create more manageable data sets for the user. The quadrants were created with 100 pixel overlaps to ensure that objects were not missed along boundaries.

#### 3.1. Master Catalogs of Sources

The first phase of our analysis focuses on creating a list of all objects detected in the six-filter summed master images. The characteristic limiting magnitudes of our master images are  $r \sim 25.5\text{--}26.0$ . The combined six-filter master images yields a greater number of faint objects than would be possible from the individual filter images. Additionally, since one of the goals of SFACT is to catalog all emission-line sources in each field, our catalog method needs to be sensitive to both nearby bright, extended sources and more distant faint, unresolved objects (and everything in between).

We utilize `DAOFIND` (Stetson 1987) for the purpose of automatically detecting every object within our survey fields. The searches are carried out by running `DAOFIND` multiple times using a series of image kernels of various sizes in order to detect objects with a range of light distributions. This allows for the identification of small compact objects as well as larger, extended galaxies. Since the multiple runs of `DAOFIND` detect most objects multiple times, we scan the final catalog and remove all duplicate entries before proceeding.

Next, we convert the image positions ( $x, y$ ) to sky coordinates (R.A., decl.), after which we carry out an identification of cross-matches within the SDSS database. While many of our objects are too faint to be identified in SDSS, for those that are we collect additional information to add to our database, including photometry and SDSS

classification (star or galaxy). After this automatic processing, we visually check the master image for bad regions to mask. This step is carried out to mitigate problems with sections of the image which, due to several nonfunctioning OTA cells, do not yield usable data. We mark these regions as a series of boxes, and any object within this region is removed from future consideration. The area contained within these masked regions is recorded in the header of the catalog table and removed from the total area of the field when doing computations involving the survey area.

It is worth stressing that our master catalog of sources can be applied to each of the individual filter images since each of these images was carefully coaligned prior to making the six-filter master image. That is, any source in the master catalog will have the same position in each of the individual filter images. Hence, this deep master catalog serves as the basis for all subsequent searches for ELGs in the individual NB images.

#### 3.2. Identifying SFACT Candidates

Once the object-cataloging phase is completed, we measure the instrumental magnitudes for every object in each NB image plus continuum image pair. We note that the NB images are not continuum subtracted and, because of the flux scaling described above, a source with no emission should have the same instrumental magnitude in both images.

The instrumental magnitudes are measured in small apertures that are set to a diameter of 3 times the FWHM of the stellar PSF relevant for each image. Since all objects in the master catalog are measured, our procedure measures isolated point sources as well as knots of emission in extended galaxies. That is, this methodology is sensitive to detecting emission-line objects regardless of their sizes or morphologies as long as the objects have been identified in our cataloging process described above. We designate these instrumental magnitudes as  $m_{\text{NB}}$  for measurements of the NB images and  $m_{\text{cont}}$  for measurements of the continuum images.

Based on these instrumental magnitudes, we next perform a secondary scaling step as a fine-tuning offset calculation. While the NB and continuum images have already been scaled to each other (see Section 2.2.2), it was found that this preliminary scaling based on typically 10–15 stars was not always accurate. Hence, a secondary scaling using our photometry for many dozens of stars was carried out. All stars which have  $m_{\text{cont}} < -10.5$  are used to compute an offset such that the median  $\Delta m = 0$  for these stars. Using the median of these offset values, a quadrant-wide offset is determined and applied to all of the objects in the table. This scaling offset is typically small, ranging between 0.00 and 0.15 mag.

Using the instrumental magnitudes, we compute the magnitude difference ( $\Delta m$ ) for each source in the catalog:

$$\Delta m = m_{\text{NB}} - m_{\text{cont}}. \quad (1)$$

We plot  $\Delta m$  versus  $m_{\text{cont}}$  for the objects in SFF01 in the left-hand plot of Figure 2. The blue dashed line designates the stars used to compute the secondary offset correction. This correction helps ensure that all of the continuum flux is properly removed in the calculation of  $\Delta m$ . We also measure a pseudo signal-to-noise ratio (henceforth referred to simply as

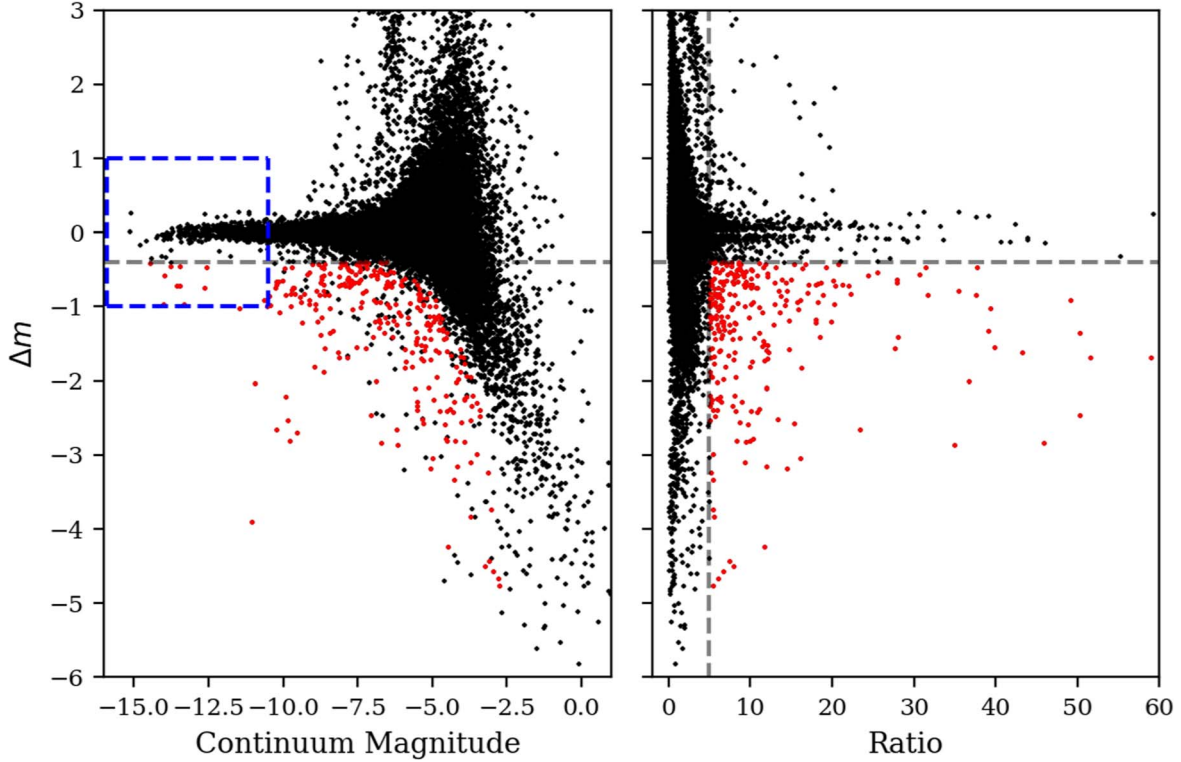


**Figure 2.** An example diagnostic plot for the SFF01 field. On the left, we plot  $\Delta m$  against the continuum magnitude. On the right, we plot the  $\Delta m$  against the *ratio*. The horizontal line represents our  $\Delta m$  cutoff of  $-0.4$ ; the vertical line represents our *ratio* cutoff of  $5.0$ . Inside the blue box in the left panel are the stars used to refine the  $\Delta m$  offsets. All objects within the lower-right section of the right plot are considered possible candidates, subject to further analysis. These objects are shown in red in both plots.

*ratio*) for each object. We use

$$\sigma_{\Delta m} = (\sigma_{\text{NB}}^2 + \sigma_{\text{cont}}^2)^{\frac{1}{2}}, \quad (2)$$

$$\text{ratio} = \frac{\Delta m}{\sigma_{\Delta m}}, \quad (3)$$

where  $\sigma_{\text{NB}}$  is the uncertainty in  $m_{\text{NB}}$  and  $\sigma_{\text{cont}}$  is the uncertainty in  $m_{\text{cont}}$ . The right-hand portion of Figure 2 plots  $\Delta m$  versus *ratio* for the objects in the SFF01 field.

We use  $\Delta m$  and *ratio* to indicate which objects have a statistically significant excess of flux in the NB filter. That is, objects with a large negative value of  $\Delta m$  have significantly more flux in the NB image than in the continuum image, while objects with larger values of *ratio* are statistically more significant. We experimented with a range of values for  $\Delta m$  and *ratio* to be used for our ELG selection criteria, running tests on multiple fields before selecting our final limits. In addition, we used our experience with previous NB emission-line surveys (e.g., Salzer et al. 2000; Kellar et al. 2012) as a guide for reasonable values for the limits. We settled upon using values of  $\Delta m$  lower than  $-0.4$  and *ratio* greater than  $5.0$  for inclusion in our ELG candidate list as providing the best balance between the desire to select candidate objects which are as faint as possible, while minimizing the number of false detections. This region of parameter space is delimited in the right-hand plot of Figure 2 by horizontal and vertical dashed lines. Objects in the lower-right section of this plot (shown in red) are ELG candidates.

The quantity  $\Delta m$  can be related directly to the equivalent width (EW) of the detected emission lines by simply applying

the definition of a magnitude:

$$\begin{aligned} \Delta m &= m_{\text{NB}} - m_{\text{cont}} = -2.5 \cdot \log \left( \frac{f_{\text{NB}}}{f_{\text{cont}}} \right) \\ &\approx -2.5 \cdot \log \left( \frac{f_{\text{line}} + f_{\text{cont}}}{f_{\text{cont}}} \right) = -2.5 \cdot \log \left( \frac{f_{\text{line}}}{f_{\text{cont}}} + 1 \right). \end{aligned} \quad (4)$$

Our  $\Delta m$  selection threshold of  $-0.4$  mag thus corresponds to a flux ratio of  $f_{\text{line}}/f_{\text{cont}} \approx 0.445$ . With our NB filter widths of  $81\text{--}97 \text{ \AA}$  (see SFACT1), the  $\Delta m$  limit corresponds to rest-frame EW selection limits of  $\sim 36\text{--}39 \text{ \AA}$  for  $\text{H}\alpha$  detections,  $\sim 27\text{--}30 \text{ \AA}$  for  $[\text{O III}]$  detections, and  $\sim 20\text{--}22 \text{ \AA}$  for  $[\text{O II}]$  detections.

The final stage in the candidate-selection process involves checking and verifying the objects identified via their  $\Delta m$  and *ratio* values. Additional scripts are used to automatically filter out obvious false detections, including saturated pixels and bleed trails associated with bright stars, image artifacts such as bad pixels, and strong cosmic rays. Once the software has selected a cleaned list of possible candidates, members of our team evaluate image cutouts created for each object (similar to what is shown in Figures 3–6). This visual inspection is carried out to ensure that the selected objects are real (i.e., not image artifacts) and that they possess a detectable amount of NB flux above the level seen in the continuum image. Each team member makes an independent decision on whether or not each object is a valid ELG candidate, and any object that is questionable is vetted by the group before a decision is made on whether or not to accept or reject it. Typically, there are of order  $100\text{--}200$  objects per



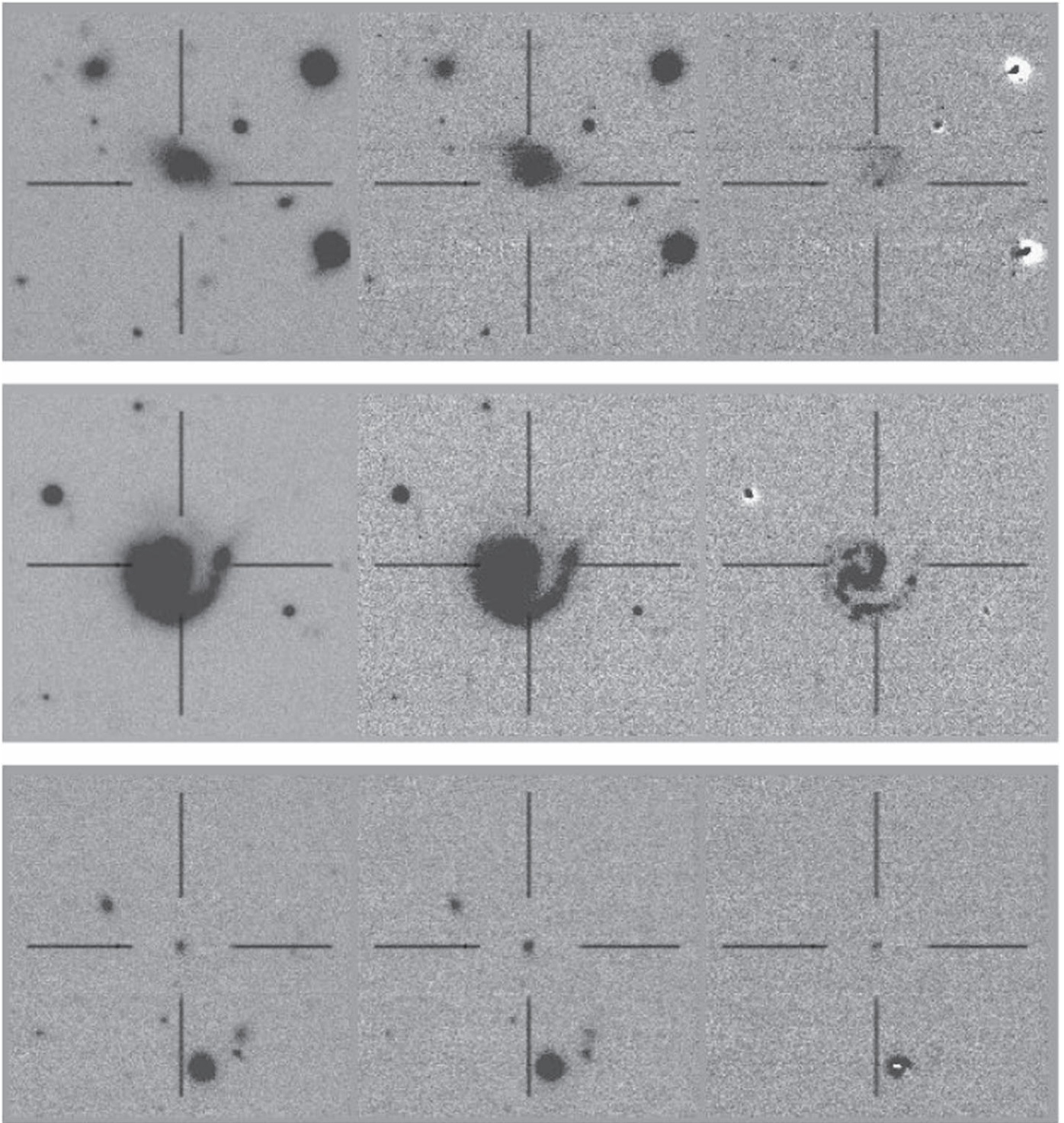


**Figure 3.** Three  $H\alpha$ -detected SFACT objects. Each row shows three  $50'' \times 50''$  image cutouts of the continuum image (left), the NB image (middle), and the difference image (right). The  $H\alpha$  redshift windows detect objects in the range  $0.0 < z < 0.15$  and include all of our extended galaxies. Top: SFF01-NB2-B19198 was detected in the NB2 filter and is a low-luminosity dwarf galaxy with  $z = 0.0034$ . Middle: SFF15-NB1-A2606 was detected in the NB1 filter via its many H II regions ( $z = 0.0643$ ). Bottom: SFF01-NB3-D2175 was detected in the NB3 filter and has  $z = 0.1374$ .

field per filter identified as SFACT candidates by our automated software, but approximately 50%–75% are rejected as spurious during this manual checking process. Most of these are image artifacts.

Because of the way the SFACT survey is carried out, we often detect multiple H II regions in a single spiral galaxy. This

applies only to the relatively low-redshift  $H\alpha$ -detected objects ( $z < 0.15$ ). The SFACT program is primarily concerned with the global properties of each ELG, rather than carrying out an accounting of each H II region. Therefore, we do not retain every single H II region in our final catalog of sources. As discussed in [SFACT1](#), we retain only the most prominent H II



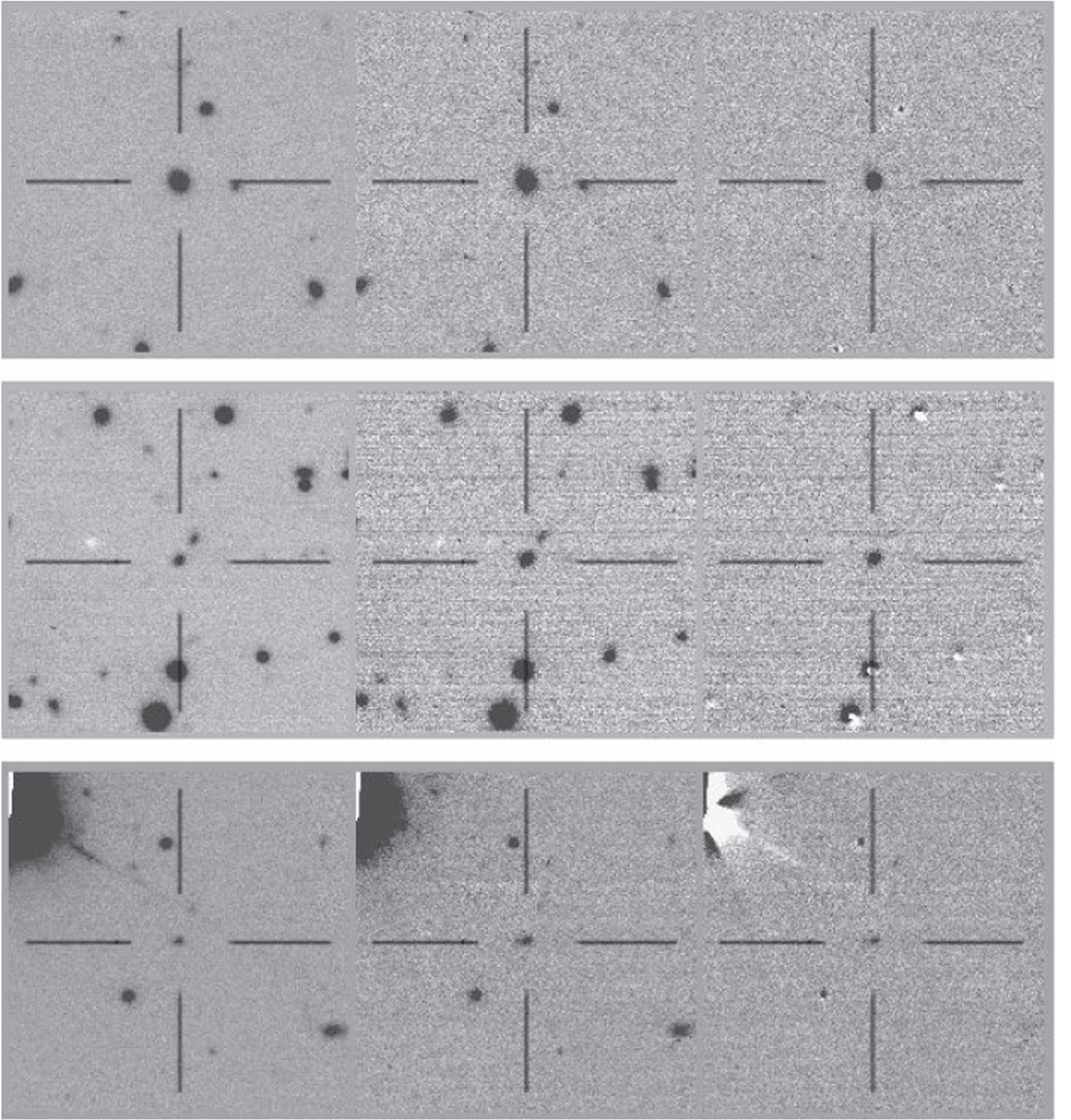


**Figure 4.** Three [O III]-detected objects. Each row shows three  $50'' \times 50''$  image cutouts of the continuum image (left), the NB image (middle), and the difference image (right). The [O III] redshift windows detect objects in the range  $0.31 < z < 0.50$ , and the [O III]-detected objects are typically compact sources like these. Top: SFF15-NB2-C20849 was detected in the NB2 filter; it is a Seyfert 2 galaxy at  $z = 0.3228$ . Middle: SFF01-NB1-D4500 was detected in the NB1 filter and is a star-forming galaxy at  $z = 0.3906$ . Bottom: SFF10-NB3-D13569 was detected in the NB3 filter at  $z = 0.4829$ .

region as a target for spectroscopic follow-up, and we use the center of the galaxy for carrying out global photometry. The lists of the individual H II regions are retained and may become part of a separate study in the future.

Following the procedures specified in this section, we arrived at final catalogs of ELG candidates for the three pilot-study fields. We detected 132 SFACT objects in SFF01, 216 in

SFF10, and 185 in SFF15. All of these objects are then slated for spectroscopic observation, as discussed in SFACT3.

### 3.3. Photometry

After the object selection is complete, we perform photometry of the SFACT candidates in the three BB (*gri*) images, as



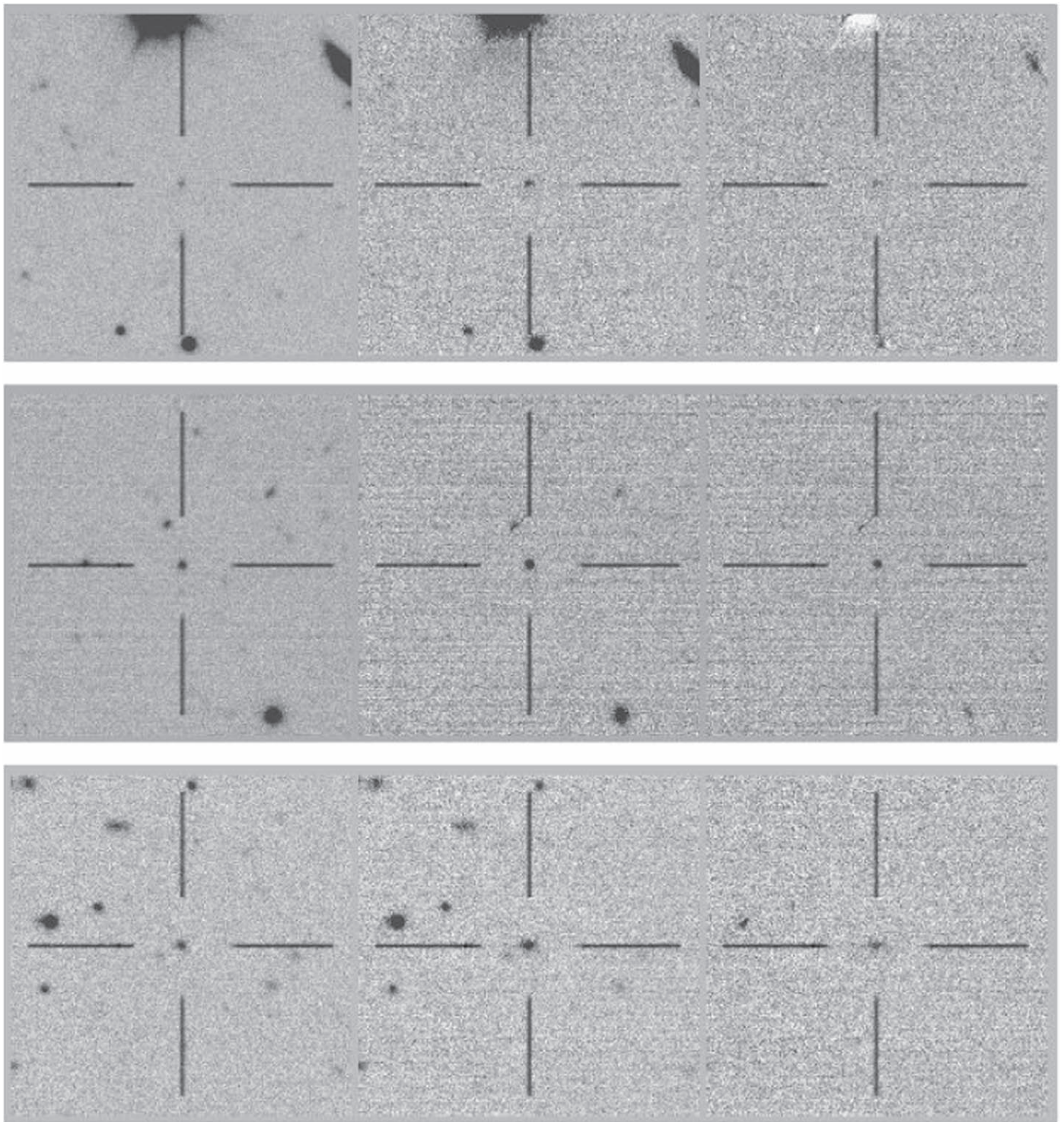


**Figure 5.** Three [O II]-detected objects. Each row shows three  $50'' \times 50''$  image cutouts of the continuum image (left), the NB image (middle), and the difference image (right). The [O II] redshift windows detect objects in the range  $0.78 < z < 1.0$  and are typically small dots like these. Top: SFF10-NB2-A8098 was detected in the NB2 filter ( $z = 0.7670$ ). Middle: SFF10-NB1-C19716 was detected in the NB1 filter and has  $z = 0.8694$ . Bottom: SFF01-NB3-B5847 was found in the NB3 filter ( $z = 1.0023$ ).

well as the relevant continuum-subtracted NB image. Here we discuss our method for performing the calibration of the BB instrumental magnitudes, the two-step process for correctly putting the NB fluxes on an appropriate flux scale, and our procedure for determining accurate brightness measurements for all SFACT targets.

### 3.3.1. Calibration

All SFACT imaging products are calibrated utilizing photometric information from SDSS stars present in our science images. For this purpose, we limit the use of SDSS stars to those with  $r$ -band magnitudes brighter than 20.0 and a  $g - r$  color in the range 0.4–1.1. We further restrict the sample



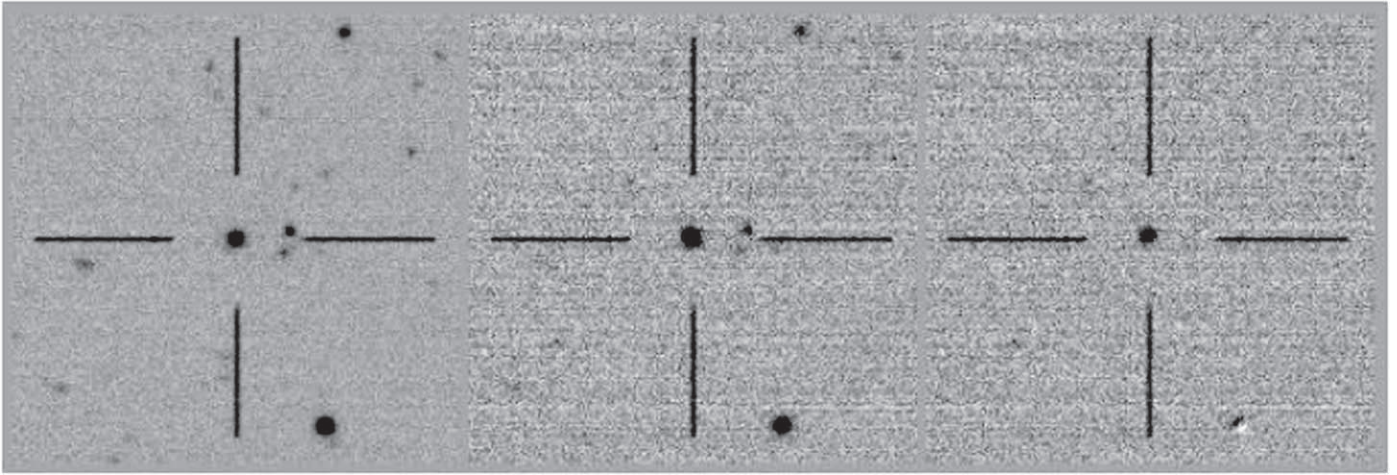


**Figure 6.** SFF10-NB2-C21205. Shown are three  $50'' \times 50''$  image cutouts of the continuum image (left), the NB image (middle), and the difference image (right). This object was detected due its strong C III] line at  $1908 \text{ \AA}$  falling in the NB2 filter. Follow-up spectra reveal it to be a quasar at  $z = 2.464$ .

of SDSS stars in each filter by an upper limit on the photometric error, typically between 0.02 and 0.03 mag. There exist sufficient numbers of stars in each field that satisfy these criteria to ensure robust photometric calibrations. We perform aperture photometry on each SDSS star and compare the derived instrumental magnitudes with the tabulated SDSS photometry, providing a difference value for each calibration star ( $\Delta m(\text{SDSS})$ ). We compute the mean and standard deviation of the  $\Delta m(\text{SDSS})$  values for all stars in each filter, retaining those within  $3\sigma$ , iterating this once to remove outliers. This cleaned sample contains hundreds of stars in each BB and NB filter. A final mean  $\Delta m(\text{SDSS})$  for each filter is calculated for this clean sample and used as the zero-point constant (ZPC) of the entire field (ZPC(SDSS)).

In order to evaluate the homogeneity of the SDSS-based calibration across our spatially large images, we divide each field into nine sections. Each section of the image typically has several dozen stars per filter. In each section, we compute the mean difference of the stars: a section-specific ZPC(SDSS). In our three pilot fields, no significant positional differences in the ZPC values across the images have been found. Most variations between the nine sections are less than  $\pm 0.01$  mag.

We also utilize the section-specific ZPC(SDSS) values to derive an estimate of the uncertainty of the overall ZPC(SDSS) for each field. This is done because computing a formal uncertainty in the main ZPC by adopting a more traditional  $\sigma/\sqrt{N}$  type error in the mean results in an unphysically small ZPC uncertainty due to the large number of SDSS stars in each field. As an alternative, we determine the standard deviation of the means in each of the nine sections. This standard deviation is used as our estimate of the uncertainty in the ZPC(SDSS) of the entire field for each filter. Characteristic uncertainties range between 0.005 and 0.015 mag for both the BB and NB filters.

Due to the narrow filter bandwidth, NB photometric calibrations traditionally do not use a color term (e.g., Kennicutt et al. 2008), a convention followed by this study. For BB photometry, we expected the color terms to be extremely small since the filters utilized are similar to those used by SDSS. We used our measurements from the pilot-study fields to verify that the color terms for the  $r$  and  $i$  filters are vanishingly small. The color term for  $g$  is somewhat larger ( $\epsilon_g = 0.105 \pm 0.002$ ), and we have applied it to our  $g$ -band magnitudes.

### 3.3.2. Narrowband Offset Calibration

The calibration of our NB flux measurements requires an additional step. This step utilizes observations of spectrophotometric standard stars (e.g., Oke & Gunn 1983; Massey et al. 1988) that were observed through each of our NB filters. In the NB SFACT science images, we perform the initial calibration using the SDSS stars just like what is performed on the BB images. This produces a magnitude difference between our SFACT objects and the SDSS stars. Because the instrumental magnitudes are measured in the same image, time-dependent quantities such as atmospheric extinction are effectively accounted for.

To properly place our NB measurements on an appropriate flux scale, we then perform an additional offset calibration utilizing observations of spectrophotometric standard stars. We repeat the same measurement procedure described above using the spectrophotometric standard stars as the “science target” and the SDSS stars found in the standard star images as the calibration sources. We arrive at a magnitude difference between the SDSS stars and our standard star. Because we employ the same filters for the science images and the calibration images, the ZPC of the SDSS stars will be the same. We can make use of this equivalence to place our NB measurements on an absolute flux scale. The offset calibration derived in this way ranges from 0.13 to 0.33 mag for the three NB filters. This offset calibration is applied on a filter by filter basis to all SFACT objects to complete the NB calibration.

### 3.3.3. Aperture Photometry

We perform photometric measurements on each SFACT object using a range of apertures. The aperture-determination step is performed on the master image in order to determine the proper BB photometric aperture for each object. We carry out a curve-of-growth analysis to determine the optimal aperture to use. Photometry is then performed on each of the individual filter images using the appropriate aperture.

Because many H II regions are located in extended galaxies, appearing as multiple knots of emission, determining the correct aperture to use is a challenge. Moreover, light from the rest of the galaxy will always be conflated with the light from the H II region. For the sake of uniformity, all H II regions are assigned the same aperture of 16 pixels ( $4''$ ). This size has been

chosen through trial and error since it adequately encapsulates the light from each individual H II region. While we measure and record the photometric properties of the individual H II regions, for most applications we utilize the measurements obtained for the entire galaxy.

If the curve-of-growth analysis in our script does not converge on an aperture to use, we examine the object by eye. We display a tiled image of each BB filter image as well as the master image overlaid with the suggested aperture. We use an interactive process to manually select an aperture which best captures the light from the target. We also inspect and confirm the apertures of sources that have near neighbors to avoid possible contamination of the photometry from the nearby source. Once we have instrumental magnitudes in all of the BB filters, we apply the ZPCs previously calculated, which puts our objects on the same magnitude scale as SDSS.

Based on the results of our BB photometry, we are able to establish the depths of our individual BB images. Characteristic  $3\sigma$  limiting magnitudes for the SFACT images are 24.4 mag in the  $r$  band, 24.0 in the  $i$  band, and 25.5 in the  $g$  band.

The photometric measurement process used for the NB images follows a procedure similar to the one described above for the BB data, with only minor differences. The curve-of-growth analysis is performed only on the continuum-subtracted NB image corresponding to the NB filter the ELG was detected in. This ensures that we are determining an aperture based on an image that contains only the emission-line flux we want to measure. Once again, we visually check the aperture of any target where the curve-of-growth software does not yield a robust solution. Once the final NB instrumental magnitudes are measured, we apply the NB ZPC calculated in the same way as the BB ZPC. We also apply the NB calibration offset described in Section 3.3.2 to place our NB measurements on a proper flux scale. Our NB magnitudes are then converted into line fluxes using the calibration from Massey et al. (1988):  $m_\nu = -2.5 \cdot \log(f_\nu) - 48.29$ .

## 4. Results

### 4.1. SFACT Survey Catalogs

We present the full list of our SFACT sources from our pilot-study fields in Tables 2–4. In each table, column (1) is the SFACT ID, the unique identifier by which we refer to any candidate. This ID is made up of the field name (ex: SFF01), the filter designation (ex: NB3), the quadrant in which the object was found (ex: D), and a running number which is assigned in the initial object-detection stage (ex: 20110). Together these quantities form the SFACT ID SFF01-NB3-D20110. We use the SFACT object ID to refer to specific sources throughout the remainder of this paper. Column (2) provides an alternate coordinate-based designation, using IAU-approved nomenclature. Columns (3) and (4) give the astrometric positions of the object in J2000 coordinates on the Gaia astrometric system. Comparison of the coordinates of stars found in the SFACT images with those cataloged in the SDSS shows that there is little or no systematic offsets between the two sets of coordinates (mean  $\Delta\alpha$  and  $\Delta\delta \leq 0''.05$  for each field), and that the rms scatter for individual stars is  $\sim 0''.15$ – $0''.20$ .

Columns (5) and (6) give the  $\Delta m$  and *ratio* values used to select candidates (see Section 3.2). Column (7) is the type of object, which is assigned during the selection process. Three

types of objects are identified: H II regions in an extended galaxy (marked as H II), the centers of any extended galaxy (ExtG), and generic emission-line objects (ELG). A detailed explanation of these types is given below. Columns (8) through (10) are the BB magnitudes measured in the  $r$ ,  $i$ , and  $g$  filters, respectively, along with their formal uncertainties. Finally, the emission-line flux in the relevant NB filter is tabulated in column (11).

The tables are sorted by the R.A. order of the objects within each field. All magnitudes and fluxes are the observed values. No corrections for Galactic absorption have been applied. Additionally, no corrections have been applied to the emission-line flux listed in column (11), either for any additional emission lines that might be present in the NB filter (e.g., [N II] emission) or for bandpass corrections. These corrections will be applied whenever appropriate in any subsequent analysis of the survey data.

SFACT is designed to be a comprehensive survey for extragalactic objects with emission lines. We detect many nearby, resolved galaxies via their individual H II regions, more distant galaxies via their “global” emission, as well as unresolved sources of emission. At the stage of creating the catalogs of our emission-line objects we do not possess any spectroscopic follow-up information, so all compact or unresolved emission-line candidates are labeled simply as ELG (even when subsequent spectroscopy reveals them to be QSOs). As is detailed in SFACT1 and mentioned in Section 3.2, for objects detected via their disk H II regions we will only catalog the brightest emission region present. These objects are labeled as H II objects in column 7 of Tables 2–4. However, for the purpose of measuring the total emission-line flux (for total star formation rates) and the total systemic BB photometry, we always catalog the central position of all galaxies that were detected via their disk H II regions. These objects are labeled as ExtG objects (for extended galaxies) in column 7.

We stress that the ExtG objects *are* ELGs, but for the purposes of our survey methodology we need to distinguish them from the more generic ELGs and from the H II regions. They do not represent a new or different class of object. All H II objects in our catalogs will have a corresponding ExtG catalog entry. However, not all ExtG objects will have a related H II object if the line emission at the center of the galaxy is the strongest emitting region in the galaxy. There are 474 objects labeled as ELG, 40 labeled as ExtG, and 19 labeled as H II in Tables 2–4.

There are 533 total SFACT objects in these three pilot-study fields. A total of  $1.50 \text{ deg}^2$  on the sky was searched. Counting only unique objects (i.e., not double counting the 19 H II regions and the corresponding galaxy centers), this gives us a surface density of  $342.7 \text{ SFACT objects deg}^{-2}$ .

### 4.2. Example Objects

We illustrate the types of objects detected in our survey by showing ten examples of SFACT candidates. These are all objects which were selected for follow-up spectroscopy and have been confirmed to be real detections. We have chosen examples which demonstrate the variety of objects found in the SFACT catalog and the depth of our images. The example objects have been grouped by their detected line. For each object, the redshift and type of object is derived from spectral analysis. This is discussed in SFACT3, where the



**Table 2**  
SFF01 Emission-line Objects

SFACT Object ID	SFACT Coordinate ID	$\alpha$ (J2000) (H:M:S)	$\delta$ (J2000) (D:M:S)	$\Delta m$ (mag)	<i>Ratio</i> (6)	Object Type (7)	$m_r$ (mag) (8)	$m_i$ (mag) (9)	$m_g$ (mag) (10)	$\log(f_{\text{NB}})$ ( $\text{erg s}^{-1} \text{cm}^{-2}$ ) (11)
(1)	(2)	(3)	(4)	(5)	(6)	(7)	(8)	(9)	(10)	(11)
SFF01-NB3-D20110	SFACT J214123.25+200510.7	21:41:23.25	20:05:10.7	$-0.57 \pm 0.02$	30.80	ExtG	$18.378 \pm 0.011$	$18.031 \pm 0.009$	$18.972 \pm 0.009$	$-14.028 \pm 0.009$
SFF01-NB3-D20084	SFACT J214123.34+200509.5	21:41:23.34	20:05:09.5	$-0.93 \pm 0.02$	45.73	H II	$19.370 \pm 0.012$	$19.030 \pm 0.011$	$19.841 \pm 0.011$	$-14.262 \pm 0.009$
SFF01-NB3-D19969	SFACT J214123.61+201118.8	21:41:23.61	20:11:18.8	$-0.64 \pm 0.10$	6.35	ELG	$21.733 \pm 0.057$	$21.706 \pm 0.089$	$22.537 \pm 0.064$	$-15.484 \pm 0.076$
SFF01-NB3-B20552	SFACT J214126.31+195845.4	21:41:26.31	19:58:45.4	$-0.37 \pm 0.01$	25.23	ExtG	$18.323 \pm 0.010$	$17.868 \pm 0.007$	$19.101 \pm 0.008$	$-14.395 \pm 0.012$
SFF01-NB1-B20542	SFACT J214126.46+194344.1	21:41:26.46	19:43:44.1	$-0.76 \pm 0.12$	6.47	ELG	$22.904 \pm 0.072$	$22.683 \pm 0.098$	$23.567 \pm 0.087$	$-15.667 \pm 0.056$
SFF01-NB2-D19115	SFACT J214126.46+201342.6	21:41:26.46	20:13:42.6	$-0.47 \pm 0.03$	14.98	ELG	$20.313 \pm 0.016$	$19.781 \pm 0.016$	$21.779 \pm 0.028$	$-14.965 \pm 0.018$
SFF01-NB3-B20497	SFACT J214126.52+195850.3	21:41:26.52	19:58:50.3	$-0.49 \pm 0.02$	20.91	ExtG	$19.083 \pm 0.011$	$18.773 \pm 0.011$	$19.553 \pm 0.010$	$-14.484 \pm 0.016$
SFF01-NB3-B19399	SFACT J214131.74+195847.3	21:41:31.74	19:58:47.3	$-0.64 \pm 0.02$	30.05	ELG	$19.215 \pm 0.013$	$18.858 \pm 0.013$	$19.701 \pm 0.012$	$-14.376 \pm 0.012$
SFF01-NB2-D17902	SFACT J214132.16+202146.6	21:41:32.16	20:21:46.6	$-0.70 \pm 0.09$	7.96	ELG	$22.346 \pm 0.093$	$21.566 \pm 0.071$	$22.880 \pm 0.095$	$-15.285 \pm 0.045$
SFF01-NB2-B19207	SFACT J214132.90+193945.5	21:41:32.90	19:39:45.5	$0.17 \pm 0.05$	3.34	ExtG	$18.747 \pm 0.014$	$18.626 \pm 0.017$	$18.951 \pm 0.010$	$-14.649 \pm 0.022$
SFF01-NB2-B19198	SFACT J214132.93+193942.1	21:41:32.93	19:39:42.1	$-0.61 \pm 0.07$	8.14	H II	$21.146 \pm 0.036$	$21.086 \pm 0.044$	$21.451 \pm 0.033$	$-15.377 \pm 0.039$
SFF01-NB1-B19076	SFACT J214133.33+194226.7	21:41:33.33	19:42:26.7	$-0.82 \pm 0.14$	6.01	ELG	$23.427 \pm 0.119$	$22.639 \pm 0.096$	$23.351 \pm 0.071$	$-15.726 \pm 0.069$
SFF01-NB3-B18885	SFACT J214134.29+194341.1	21:41:34.29	19:43:41.1	$-0.97 \pm 0.10$	9.97	ELG	$22.740 \pm 0.058$	$22.380 \pm 0.071$	$22.924 \pm 0.053$	$-15.419 \pm 0.035$
SFF01-NB3-B18561	SFACT J214135.87+194757.5	21:41:35.87	19:47:57.5	$-0.69 \pm 0.13$	5.12	ELG	$23.252 \pm 0.101$	$22.674 \pm 0.109$	$23.708 \pm 0.105$	$-15.776 \pm 0.062$
SFF01-NB2-B18506	SFACT J214136.06+195653.7	21:41:36.06	19:56:53.7	$-0.81 \pm 0.15$	5.52	ELG	$23.401 \pm 0.108$	$23.098 \pm 0.139$	$23.873 \pm 0.109$	$-15.804 \pm 0.050$
SFF01-NB3-B18371	SFACT J214136.92+193734.2	21:41:36.92	19:37:34.2	$-1.30 \pm 0.17$	7.60	ELG	$23.484 \pm 0.119$	$23.154 \pm 0.140$	$23.727 \pm 0.097$	$-15.574 \pm 0.047$
SFF01-NB3-B17245	SFACT J214141.87+195707.7	21:41:41.87	19:57:07.7	$-1.02 \pm 0.14$	7.27	ELG	$22.817 \pm 0.073$	$22.685 \pm 0.108$	$22.971 \pm 0.059$	$-15.452 \pm 0.051$
SFF01-NB3-D15415	SFACT J214142.73+201252.3	21:41:42.73	20:12:52.3	$-0.68 \pm 0.10$	6.89	ELG	$22.246 \pm 0.055$	$22.249 \pm 0.090$	$22.786 \pm 0.067$	$-15.581 \pm 0.058$
SFF01-NB2-D15191	SFACT J214143.48+200448.4	21:41:43.48	20:04:48.4	$-0.61 \pm 0.08$	7.47	ELG	$21.655 \pm 0.049$	$21.398 \pm 0.062$	$22.484 \pm 0.059$	$-15.466 \pm 0.046$
SFF01-NB1-B16317	SFACT J214146.59+194328.3	21:41:46.59	19:43:28.3	$-0.75 \pm 0.11$	6.97	ELG	$22.463 \pm 0.086$	$22.048 \pm 0.097$	$22.913 \pm 0.092$	$-15.647 \pm 0.056$
SFF01-NB3-B16011	SFACT J214148.07+195758.9	21:41:48.07	19:57:58.9	$-1.10 \pm 0.11$	10.46	ELG	$22.690 \pm 0.056$	$22.609 \pm 0.087$	$23.057 \pm 0.057$	$-15.367 \pm 0.038$
SFF01-NB3-B15732	SFACT J214149.54+194038.6	21:41:49.54	19:40:38.6	$-0.67 \pm 0.10$	6.99	ELG	$22.540 \pm 0.070$	$22.134 \pm 0.074$	$22.934 \pm 0.061$	$-15.548 \pm 0.065$
SFF01-NB2-B15722	SFACT J214149.60+193848.3	21:41:49.60	19:38:48.3	$-0.42 \pm 0.07$	5.56	ELG	$22.185 \pm 0.058$	$21.341 \pm 0.044$	$23.128 \pm 0.077$	$-15.670 \pm 0.054$
SFF01-NB1-D13076	SFACT J214150.05+200728.2	21:41:50.05	20:07:28.2	$-0.96 \pm 0.13$	7.26	ELG	$23.247 \pm 0.104$	$22.684 \pm 0.110$	$23.800 \pm 0.113$	$-15.705 \pm 0.053$
SFF01-NB1-D12776	SFACT J214150.91+202341.9	21:41:50.91	20:23:41.9	$-0.51 \pm 0.08$	6.04	ELG	$22.214 \pm 0.085$	$21.255 \pm 0.053$	$23.238 \pm 0.114$	$-15.577 \pm 0.057$
SFF01-NB3-B14965	SFACT J214153.12+195235.0	21:41:53.12	19:52:35.0	$-0.42 \pm 0.03$	14.55	ELG	$19.891 \pm 0.016$	$19.600 \pm 0.019$	$20.436 \pm 0.016$	$-14.907 \pm 0.021$
SFF01-NB3-B14799	SFACT J214153.89+195227.9	21:41:53.89	19:52:27.9	$-0.62 \pm 0.11$	5.74	ELG	$22.701 \pm 0.072$	$22.138 \pm 0.075$	$22.944 \pm 0.066$	$-15.595 \pm 0.059$
SFF01-NB3-D11444	SFACT J214155.02+201511.4	21:41:55.02	20:15:11.4	$-0.65 \pm 0.09$	7.22	ELG	$22.600 \pm 0.050$	$22.323 \pm 0.063$	$23.024 \pm 0.060$	$-15.619 \pm 0.047$
SFF01-NB2-B14205	SFACT J214156.04+195310.0	21:41:56.04	19:53:10.0	$-0.83 \pm 0.08$	10.89	ELG	$21.993 \pm 0.048$	$21.888 \pm 0.069$	$22.616 \pm 0.054$	$-15.308 \pm 0.031$
SFF01-NB1-D10796	SFACT J214157.21+201512.0	21:41:57.21	20:15:12.0	$-0.92 \pm 0.10$	9.25	ELG	$22.868 \pm 0.068$	$22.466 \pm 0.073$	$25.806 \pm 0.509$	$-15.471 \pm 0.044$

(This table is available in its entirety in machine-readable form.)

**Table 3**  
SFF10 Emission-line Objects

SFACT Object ID	SFACT Coordinate ID	$\alpha$ (J2000) (H:M:S)	$\delta$ (J2000) (D:M:S)	$\Delta m$ (mag)	Ratio	Object Type	$m_r$ (mag)	$m_i$ (mag)	$m_g$ (mag)	$\log(f_{\text{NB}})$ ( $\text{erg s}^{-1} \text{cm}^{-2}$ )
(1)	(2)	(3)	(4)	(5)	(6)	(7)	(8)	(9)	(10)	(11)
SFF10-NB3-D13755	SFACT J014256.70+281615.3	1:42:56.70	28:16:15.3	$-1.72 \pm 0.28$	6.26	ELG	$25.846 \pm 0.986$	$24.064 \pm 0.189$	$25.491 \pm 0.370$	$-15.572 \pm 0.053$
SFF10-NB3-D13569	SFACT J014258.14+275740.4	1:42:58.14	27:57:40.4	$-0.72 \pm 0.08$	8.46	ELG	$22.157 \pm 0.087$	$22.058 \pm 0.073$	$23.037 \pm 0.074$	$-15.299 \pm 0.038$
SFF10-NB2-B12883	SFACT J014258.90+274309.1	1:42:58.90	27:43:09.1	$-1.12 \pm 0.17$	6.55	ELG	$23.580 \pm 0.167$	$23.307 \pm 0.129$	$24.395 \pm 0.140$	$-15.716 \pm 0.065$
SFF10-NB3-B12772	SFACT J014259.69+274052.3	1:42:59.69	27:40:52.3	$-0.52 \pm 0.09$	5.57	ELG	$22.981 \pm 0.126$	$22.067 \pm 0.063$	$24.609 \pm 0.216$	$-15.558 \pm 0.063$
SFF10-NB3-D13083	SFACT J014300.87+280623.8	1:43:00.87	28:06:23.8	$-1.18 \pm 0.10$	11.59	ELG	$22.741 \pm 0.127$	$22.534 \pm 0.099$	$23.547 \pm 0.107$	$-15.414 \pm 0.032$
SFF10-NB1-B12579	SFACT J014300.97+274122.1	1:43:00.97	27:41:22.1	$-0.52 \pm 0.08$	6.62	ELG	$22.108 \pm 0.070$	$21.398 \pm 0.040$	$22.774 \pm 0.058$	$-15.518 \pm 0.050$
SFF10-NB3-B12471	SFACT J014301.74+273928.5	1:43:01.74	27:39:28.5	$-0.61 \pm 0.11$	5.39	ELG	$23.218 \pm 0.123$	$22.704 \pm 0.078$	$23.677 \pm 0.085$	$-15.722 \pm 0.064$
SFF10-NB1-D12909	SFACT J014302.15+281152.9	1:43:02.15	28:11:52.9	$-0.45 \pm 0.04$	10.02	ExtG	$20.319 \pm 0.028$	$20.137 \pm 0.025$	$21.015 \pm 0.025$	$-14.911 \pm 0.026$
SFF10-NB3-B12244	SFACT J014303.57+273655.2	1:43:03.57	27:36:55.2	$-1.09 \pm 0.13$	8.16	ELG	$23.287 \pm 0.161$	$23.030 \pm 0.124$	$24.274 \pm 0.151$	$-15.572 \pm 0.046$
SFF10-NB2-B12225	SFACT J014303.75+273744.4	1:43:03.75	27:37:44.4	$-1.04 \pm 0.12$	8.91	ELG	$22.974 \pm 0.150$	$22.436 \pm 0.089$	$23.421 \pm 0.094$	$-15.520 \pm 0.043$
SFF10-NB3-B12131	SFACT J014304.20+275025.1	1:43:04.20	27:50:25.1	$-0.87 \pm 0.04$	22.34	ELG	$20.993 \pm 0.030$	$20.699 \pm 0.025$	$21.551 \pm 0.026$	$-14.830 \pm 0.016$
SFF10-NB3-B12081	SFACT J014304.52+275030.9	1:43:04.52	27:50:30.9	$-0.59 \pm 0.03$	18.35	ELG	$20.137 \pm 0.024$	$19.879 \pm 0.019$	$20.772 \pm 0.021$	$-14.802 \pm 0.015$
SFF10-NB1-B12096	SFACT J014304.64+273418.2	1:43:04.64	27:34:18.2	$-0.59 \pm 0.09$	6.66	ELG	$22.348 \pm 0.087$	$21.572 \pm 0.046$	$22.685 \pm 0.054$	$-15.453 \pm 0.057$
SFF10-NB3-D12508	SFACT J014305.18+275632.9	1:43:05.18	27:56:32.9	$-0.70 \pm 0.12$	5.66	ELG	$23.594 \pm 0.281$	$22.564 \pm 0.111$	$23.301 \pm 0.099$	$-15.670 \pm 0.073$
SFF10-NB3-B11870	SFACT J014306.06+274431.6	1:43:06.06	27:44:31.6	$-0.75 \pm 0.13$	5.68	ELG	$23.412 \pm 0.145$	$22.970 \pm 0.093$	$24.131 \pm 0.116$	$-15.742 \pm 0.064$
SFF10-NB3-B11533	SFACT J014307.68+275244.6	1:43:07.68	27:52:44.6	$-0.48 \pm 0.09$	5.36	ELG	$22.565 \pm 0.100$	$22.222 \pm 0.077$	$22.888 \pm 0.065$	$-15.623 \pm 0.049$
SFF10-NB3-D12024	SFACT J014308.50+281103.9	1:43:08.50	28:11:03.9	$-0.64 \pm 0.12$	5.16	ELG	$23.389 \pm 0.117$	$22.811 \pm 0.075$	$24.237 \pm 0.106$	$-15.860 \pm 0.063$
SFF10-NB2-D11997	SFACT J014308.81+281226.9	1:43:08.81	28:12:26.9	$-0.88 \pm 0.13$	6.71	ELG	$22.853 \pm 0.129$	$23.009 \pm 0.170$	$23.441 \pm 0.097$	$-15.653 \pm 0.062$
SFF10-NB3-D11938	SFACT J014309.34+280305.7	1:43:09.34	28:03:05.7	$-1.41 \pm 0.09$	16.23	ELG	$21.941 \pm 0.079$	$21.785 \pm 0.066$	$22.297 \pm 0.051$	$-15.029 \pm 0.032$
SFF10-NB3-D11925	SFACT J014309.51+275434.0	1:43:09.51	27:54:34.0	$-0.47 \pm 0.09$	5.42	ELG	$22.771 \pm 0.137$	$21.581 \pm 0.046$	$22.368 \pm 0.045$	$-15.727 \pm 0.057$
SFF10-NB3-B11195	SFACT J014309.97+273813.9	1:43:09.97	27:38:13.9	$-0.87 \pm 0.13$	6.67	ELG	$23.137 \pm 0.123$	$22.993 \pm 0.103$	$23.567 \pm 0.081$	$-15.608 \pm 0.055$
SFF10-NB3-D11772	SFACT J014310.63+280641.6	1:43:10.63	28:06:41.6	$-1.91 \pm 0.22$	8.82	ELG	$24.347 \pm 0.311$	$23.978 \pm 0.219$	$25.532 \pm 0.377$	$-15.512 \pm 0.042$
SFF10-NB1-B10986	SFACT J014311.40+273300.7	1:43:11.40	27:33:00.7	$-1.21 \pm 0.12$	9.93	ELG	$23.077 \pm 0.135$	$22.663 \pm 0.083$	$23.290 \pm 0.069$	$-15.392 \pm 0.039$
SFF10-NB1-B10674	SFACT J014313.32+274124.6	1:43:13.32	27:41:24.6	$-0.75 \pm 0.04$	16.69	ELG	$21.134 \pm 0.038$	$20.823 \pm 0.030$	$21.422 \pm 0.026$	$-15.008 \pm 0.022$
SFF10-NB2-B10675	SFACT J014313.39+273356.3	1:43:13.39	27:33:56.3	$-0.47 \pm 0.06$	7.38	ELG	$21.985 \pm 0.054$	$21.429 \pm 0.035$	$22.725 \pm 0.046$	$-15.493 \pm 0.041$
SFF10-NB1-D11121	SFACT J014315.23+280125.9	1:43:15.23	28:01:25.9	$-1.00 \pm 0.09$	10.82	ELG	$22.779 \pm 0.089$	$22.039 \pm 0.049$	$23.259 \pm 0.061$	$-15.322 \pm 0.037$
SFF10-NB3-D11032	SFACT J014315.47+281521.9	1:43:15.47	28:15:21.9	$-1.27 \pm 0.06$	19.98	ELG	$21.873 \pm 0.070$	$21.629 \pm 0.055$	$22.815 \pm 0.055$	$-14.941 \pm 0.020$
SFF10-NB3-D10890	SFACT J014316.09+275845.4	1:43:16.09	27:58:45.4	$-0.66 \pm 0.03$	20.21	H II	$20.058 \pm 0.020$	$19.625 \pm 0.015$	$20.703 \pm 0.018$	$-14.659 \pm 0.015$
SFF10-NB3-D10873	SFACT J014316.14+275843.3	1:43:16.14	27:58:43.3	$-0.38 \pm 0.02$	17.35	ExtG	$19.055 \pm 0.019$	$18.647 \pm 0.014$	$19.811 \pm 0.016$	$-14.418 \pm 0.014$
SFF10-NB3-B10141	SFACT J014316.41+274430.5	1:43:16.41	27:44:30.5	$-1.28 \pm 0.20$	6.43	ELG	$24.082 \pm 0.250$	$23.518 \pm 0.144$	$24.358 \pm 0.137$	$-15.788 \pm 0.062$

(This table is available in its entirety in machine-readable form.)



**Table 4**  
SFF15 Emission-line Objects

SFACT Object ID	SFACT Coordinate ID	$\alpha$ (J2000) (H:M:S)	$\delta$ (J2000) (D:M:S)	$\Delta m$ (mag)	Ratio	Object Type	$m_r$ (mag)	$m_i$ (mag)	$m_g$ (mag)	$\log(f_{\text{NB}})$ ( $\text{erg s}^{-1} \text{cm}^{-2}$ )
(1)	(2)	(3)	(4)	(5)	(6)	(7)	(8)	(9)	(10)	(11)
SFF15-NB3-B14284	SFACT J023730.56+274425.1	2:37:30.56	27:44:25.1	-0.71 ± 0.10	7.11	ExtG	21.747 ± 0.068	21.774 ± 0.075	22.427 ± 0.062	-15.413 ± 0.048
SFF15-NB1-B14251	SFACT J023730.82+274059.9	2:37:30.82	27:40:59.9	-0.94 ± 0.17	5.63	ELG	23.294 ± 0.178	22.758 ± 0.113	23.926 ± 0.134	-15.741 ± 0.065
SFF15-NB2-D24348	SFACT J023731.19+281026.8	2:37:31.19	28:10:26.8	-0.68 ± 0.13	5.14	ELG	22.734 ± 0.119	22.840 ± 0.147	23.688 ± 0.127	-15.849 ± 0.094
SFF15-NB2-B14131	SFACT J023731.68+272845.4	2:37:31.68	27:28:45.4	-1.29 ± 0.21	5.99	ELG	23.378 ± 0.223	23.925 ± 0.355	24.420 ± 0.252	-15.731 ± 0.089
SFF15-NB3-B14046	SFACT J023731.96+275052.4	2:37:31.96	27:50:52.4	-0.47 ± 0.07	6.65	ELG	22.050 ± 0.047	21.716 ± 0.041	22.908 ± 0.053	-15.560 ± 0.042
SFF15-NB2-D22777	SFACT J023733.00+281011.2	2:37:33.00	28:10:11.2	-1.53 ± 0.04	34.51	ELG	21.096 ± 0.040	21.435 ± 0.057	21.788 ± 0.037	-14.644 ± 0.016
SFF15-NB2-B13724	SFACT J023734.14+274128.0	2:37:34.14	27:41:28.0	-0.79 ± 0.07	11.71	ELG	22.404 ± 0.047	22.260 ± 0.045	23.404 ± 0.058	-15.522 ± 0.030
SFF15-NB2-B13721	SFACT J023734.15+274129.1	2:37:34.15	27:41:29.1	-0.90 ± 0.06	16.11	ELG	21.621 ± 0.034	21.529 ± 0.033	22.618 ± 0.041	-15.154 ± 0.021
SFF15-NB2-D22292	SFACT J023734.35+281003.1	2:37:34.35	28:10:03.1	-0.49 ± 0.08	5.74	ELG	21.645 ± 0.074	21.500 ± 0.074	22.790 ± 0.087	-15.410 ± 0.051
SFF15-NB2-D22224	SFACT J023734.52+280514.9	2:37:34.52	28:05:14.9	-1.37 ± 0.14	9.85	ELG	23.120 ± 0.138	23.295 ± 0.166	24.012 ± 0.138	-15.597 ± 0.037
SFF15-NB3-D22277	SFACT J023734.53+275653.7	2:37:34.53	27:56:53.7	-0.49 ± 0.08	5.98	ELG	22.342 ± 0.061	21.809 ± 0.042	23.564 ± 0.077	-15.633 ± 0.048
SFF15-NB3-B13580	SFACT J023735.23+274121.9	2:37:35.23	27:41:21.9	-0.48 ± 0.05	9.76	ELG	21.423 ± 0.031	21.181 ± 0.026	21.581 ± 0.022	-15.288 ± 0.024
SFF15-NB2-D20719	SFACT J023738.93+280530.2	2:37:38.93	28:05:30.2	-0.52 ± 0.08	6.34	ELG	21.875 ± 0.059	22.076 ± 0.072	22.966 ± 0.065	-15.633 ± 0.035
SFF15-NB1-B12855	SFACT J023740.25+274942.1	2:37:40.25	27:49:42.1	-0.80 ± 0.10	7.79	ELG	22.611 ± 0.100	22.174 ± 0.072	22.864 ± 0.071	-15.550 ± 0.049
SFF15-NB2-B12874	SFACT J023740.34+272939.9	2:37:40.34	27:29:39.9	-1.17 ± 0.09	13.00	ELG	22.549 ± 0.070	22.583 ± 0.078	23.594 ± 0.078	-15.367 ± 0.029
SFF15-NB2-B12729	SFACT J023741.60+272959.4	2:37:41.60	27:29:59.4	-1.70 ± 0.14	11.94	ELG	22.939 ± 0.159	23.720 ± 0.345	23.689 ± 0.161	-15.291 ± 0.033
SFF15-NB2-D19839	SFACT J023741.93+281035.0	2:37:41.93	28:10:35.0	-0.63 ± 0.12	5.11	ELG	22.770 ± 0.097	22.906 ± 0.142	23.588 ± 0.105	-15.757 ± 0.066
SFF15-NB1-B12675	SFACT J023742.16+272938.9	2:37:42.16	27:29:38.9	-0.74 ± 0.13	5.60	ELG	22.927 ± 0.100	22.736 ± 0.083	24.033 ± 0.114	-15.662 ± 0.071
SFF15-NB3-B12608	SFACT J023742.63+274616.0	2:37:42.63	27:46:16.0	-0.51 ± 0.09	5.56	ELG	22.604 ± 0.058	22.288 ± 0.049	23.423 ± 0.065	-15.707 ± 0.054
SFF15-NB3-B12427	SFACT J023744.04+274533.7	2:37:44.04	27:45:33.7	-0.63 ± 0.05	12.28	ELG	21.254 ± 0.034	21.076 ± 0.029	22.018 ± 0.032	-15.248 ± 0.024
SFF15-NB3-D18788	SFACT J023744.26+281330.5	2:37:44.26	28:13:30.5	-0.54 ± 0.08	7.05	ELG	22.009 ± 0.051	21.968 ± 0.055	22.820 ± 0.054	-15.391 ± 0.046
SFF15-NB2-B12371	SFACT J023744.60+273441.2	2:37:44.60	27:34:41.2	-0.60 ± 0.06	9.79	ExtG	21.934 ± 0.045	21.494 ± 0.035	22.785 ± 0.045	-15.335 ± 0.030
SFF15-NB1-D18539	SFACT J023744.78+281340.3	2:37:44.78	28:13:40.3	-1.37 ± 0.10	13.44	ELG	21.511 ± 0.033	21.295 ± 0.030	23.294 ± 0.083	-15.386 ± 0.033
SFF15-NB3-B12212	SFACT J023745.92+273918.5	2:37:45.92	27:39:18.5	-0.77 ± 0.09	8.86	ELG	22.657 ± 0.075	22.226 ± 0.056	23.587 ± 0.078	-15.525 ± 0.030
SFF15-NB3-D17352	SFACT J023746.87+280421.5	2:37:46.87	28:04:21.5	-0.71 ± 0.11	6.15	ELG	24.036 ± 0.220	22.660 ± 0.069	26.318 ± 0.717	-15.750 ± 0.061
SFF15-NB3-B11965	SFACT J023747.82+274851.5	2:37:47.82	27:48:51.5	-0.75 ± 0.10	7.21	ELG	22.912 ± 0.115	22.340 ± 0.069	23.381 ± 0.075	-15.570 ± 0.057
SFF15-NB1-D15218	SFACT J023748.24+281511.6	2:37:48.24	28:15:11.6	-0.53 ± 0.10	5.22	ELG	21.954 ± 0.109	21.542 ± 0.083	23.071 ± 0.165	-15.326 ± 0.067
SFF15-NB1-D14190	SFACT J023749.21+280902.6	2:37:49.21	28:09:02.6	-0.73 ± 0.14	5.01	ELG	22.798 ± 0.126	22.347 ± 0.109	23.150 ± 0.100	-15.754 ± 0.081
SFF15-NB2-B11684	SFACT J023750.76+272858.2	2:37:50.76	27:28:58.2	-1.91 ± 0.17	11.41	ELG	23.082 ± 0.127	24.305 ± 0.440	25.051 ± 0.315	-15.383 ± 0.035
SFF15-NB3-D13288	SFACT J023751.99+275346.3	2:37:51.99	27:53:46.3	-0.65 ± 0.07	8.78	ELG	22.373 ± 0.070	21.789 ± 0.044	23.308 ± 0.072	-15.364 ± 0.042

(This table is available in its entirety in machine-readable form.)

corresponding spectra for these example objects can be found. These image cutouts are produced by our software and are used during ELG candidate evaluations and checking.

#### 4.2.1. $H\alpha$ Detections

The first three example SFACT galaxies, shown in Figure 3, were all detected via their  $H\alpha$  emission line. SFF01-NB2-B19198, at the top of Figure 3, is one of our closest ELGs at  $z=0.0034$ . The specific object is not actually the galaxy center, but an H II region near the center. As discussed in Section 3.3.3, the H II region remains in our catalog, but the photometric properties measured are those for the galaxy as a whole. Here it is visually clear that the H II region is a large knot of emission in an otherwise quiescent dwarf galaxy. In a more traditional BB-only survey this may not have stood out as a source of emission. This galaxy has a total  $g$ -band magnitude of 19.00 and a NB flux of  $2.24 \times 10^{-15} \text{ erg s}^{-1} \text{ cm}^{-2}$ .

The middle galaxy is SFF15-NB1-A2606, which was detected in our NB1 filter. Again, this is an H II region in a larger galaxy. This spiral galaxy is found at  $z=0.0643$  with a  $g$ -band magnitude of 17.16 and an integrated NB flux of  $2.36 \times 10^{-14} \text{ erg s}^{-1} \text{ cm}^{-2}$ . Both of these first two galaxies demonstrate the ability of SFACT to find H II regions in extended sources.

The last of this set is a more typical SFACT ELG. SFF01-NB3-D2175 is a compact object that is visible in the continuum image and appears slightly brighter in the NB image. This particular galaxy has a  $g$ -band magnitude of 22.41, a NB flux of  $2.80 \times 10^{-16} \text{ erg s}^{-1} \text{ cm}^{-2}$ , and is found at  $z=0.1374$ . This system is a low-luminosity dwarf star-forming galaxy.

#### 4.2.2. [O III] Detections

The next three examples, shown in Figure 4, are each [O III] detections. In the top set of images is SFF15-NB2-C20849. This galaxy has very strong line emission. In our nearest [O III] redshift window, this object is at  $z=0.3228$  with a  $g$ -band magnitude of 21.17 and a NB flux of  $6.81 \times 10^{-15} \text{ erg s}^{-1} \text{ cm}^{-2}$ , making it the object with the second strongest flux in this example set, and the strongest of those which are not large spiral galaxies. Follow-up analysis (discussed in SFACT3) has confirmed that this object is a Seyfert 2.

The middle set of images shows SFF01-NB1-D4500, which has a  $g$ -band magnitude of 22.56. This object is found at  $z=0.3906$  and has a NB flux of  $1.01 \times 10^{-15} \text{ erg s}^{-1} \text{ cm}^{-2}$ . This object represents a strong, clear detection and may be a Green Pea-like star-forming galaxy (e.g., Cardamone et al. 2009; Brunner et al. 2020).

Rounding out the [O III]-detected set is SFF10-NB3-D13569, at the bottom of Figure 4. This system is at a redshift of  $z=0.4829$  with a  $g$ -band magnitude of 23.02 and a NB flux of  $5.03 \times 10^{-16} \text{ erg s}^{-1} \text{ cm}^{-2}$ . This object is representative of many SFACT objects for which the NB flux is not overwhelmingly strong yet still have a strong enough emission line for us to clearly identify it as an object of interest.

#### 4.2.3. [O II] Detections

The final set of example objects are shown in Figure 5 and were each detected by their [O II] line. SFF10-NB2-A8098, shown in the top set of Figure 5, is one of our fainter sources at a  $g$ -band magnitude of 23.78, falling over half a magnitude below the median  $g$ -band magnitude of the pilot-study objects

(SFACT1). This demonstrates the sensitivity of SFACT. The galaxy in the NB image before continuum subtraction (the middle cutout) looks brighter than in the continuum image on the left, demonstrating the visually strong emission line. It is at a distance of  $z=0.7670$  and has a NB flux of  $2.04 \times 10^{-16} \text{ erg s}^{-1} \text{ cm}^{-2}$ .

On the middle row is SFF10-NB1-C19716. This galaxy is at  $z=0.8694$ ; at such a distance, it is understandably very compact in our images. This object has a  $g$ -band magnitude of 23.06 and a NB flux of  $3.63 \times 10^{-16} \text{ erg s}^{-1} \text{ cm}^{-2}$ .

One of the most distant galaxies in our primary redshift windows is SFF01-NB3-B5847 at  $z=1.0023$ . It has a  $g$ -band magnitude of 23.08 and a NB flux of  $4.51 \times 10^{-16} \text{ erg s}^{-1} \text{ cm}^{-2}$ .

#### 4.2.4. Other Detections

SFACT detects objects outside of our primary redshift windows, including numerous QSOs. The last example object, shown in Figure 6, is one such QSO. For this object, the C III] emission line at  $1908 \text{ \AA}$  is redshifted into our NB2 filter, allowing us to detect it. As can be seen from Figure 6, it is a bright target, with a  $g$ -band magnitude of 20.95. It exhibits a moderate line flux of  $7.94 \times 10^{-16} \text{ erg s}^{-1} \text{ cm}^{-2}$  yet its distance,  $z=2.4643$ , demonstrates SFACT's ability to detect objects well beyond  $z=1$ . There are a total of 13 objects in this pilot study that are at redshifts greater than our primary redshift windows, all of which have been verified as QSOs in our follow-up spectroscopic observations (see SFACT3).

The spectra corresponding to all of the example SFACT objects shown here can be found in SFACT3.

### 4.3. Photometric Properties of SFACT Objects

In this section, we examine the photometric properties of the SFACT objects. SFACT1 (Figure 2) presents a set of composite histograms showing the range of BB apparent magnitudes for the full sample of pilot-study candidates, demonstrating the depth of our sample. In this paper, we examine these photometric properties in more detail by comparing the distributions of BB magnitude and NB line flux across the three pilot-study fields as well as across the three NB filters.

Figure 7 shows the distribution of  $r$ -band magnitude and NB flux for each pilot-study field separately. While there are variations between the fields, the broad characteristics are very similar. The median  $r$ -band magnitudes are 22.53, 22.50, and 22.51, demonstrating a remarkably consistent depth between the fields. This figure also demonstrates the range of brightnesses in our catalog. We see objects that have an  $r$ -band magnitude as bright as 16 and as faint as 25. The NB flux distribution on the right-hand side of Figure 7 also exhibits strong similarities across the survey fields. The median log NB flux is seen to be very stable across the three fields:  $-15.51$ ,  $-15.50$ , and  $-15.57 \text{ erg s}^{-1} \text{ cm}^{-2}$ .

Figure 2 of SFACT1 also presents a composite  $g-r$  histogram. Like the BB magnitudes, there is a broad range of colors represented in the sample. The median  $g-r$  color of 0.65 is consistent with early-type spiral galaxies, but the bulk of the sample has colors between  $0.2 < g-r < 1.2$  and includes many red systems. As discussed in SFACT1, this is due in part to our selection method. Strong emission lines are present in many of our candidates, and these strong lines can influence the overall color of the galaxy, leading to an actively



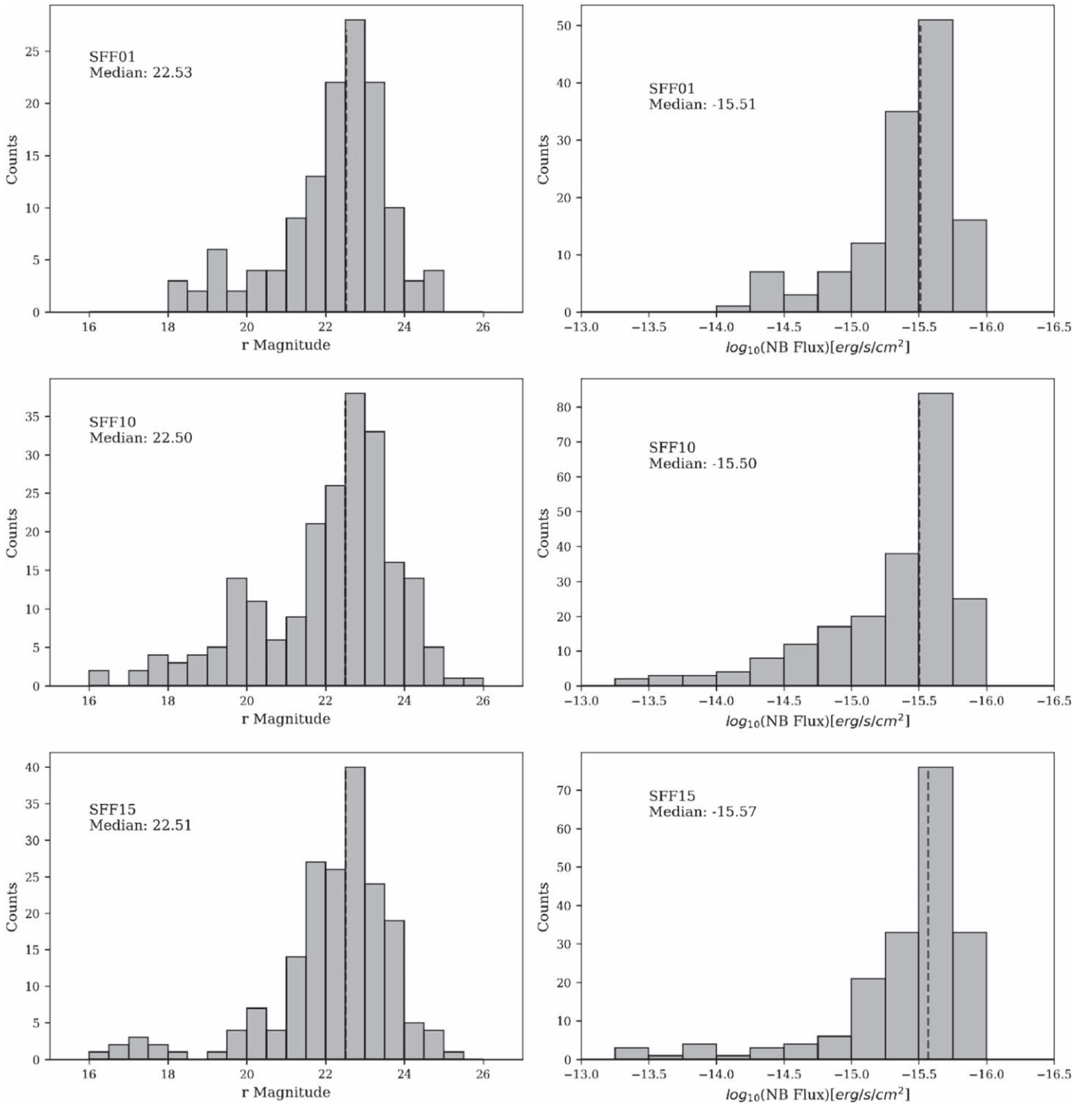


**Figure 7.** Distributions of  $r$ -band magnitude and NB flux broken down by field. The left-hand plots show the  $r$ -band magnitude distributions for each of the pilot-study fields, while the right shows the NB flux distributions. From top to bottom is SFF01, SFF10, then SFF15. The vertical dashed lines mark the median of each distribution. The distributions are seen to be very similar from field to field.

star-forming system appearing redder than expected (e.g., Cardamone et al. 2009; Yang et al. 2017). These strong emission lines can be seen as part of a wide range of emission-line strengths in Figure 7. This figure highlights SFACT’s sensitivity. The strong peak in  $\log(f_{\text{NB}})$  between  $-15.50$  and  $-15.75$  implies that our survey is complete to approximately this level.

As another way of viewing the distribution, Figure 8 shows a similar set of histograms, this time broken down according to

which NB filter the object was detected in. While there is a slightly greater spread in the median values, there is still strong consistency across the data sets. The most striking difference is the extended bright end of the distributions in NB1 and the deficit of brighter sources in NB2. The latter is presumably caused by the almost complete lack of  $\text{H}\alpha$  detections in NB2. This is expected, due to the limited volume over which any  $\text{H}\alpha$  sources could be found within the NB2 filter. Conversely, NB1 finds more  $\text{H}\alpha$ -detected galaxies that are bright.

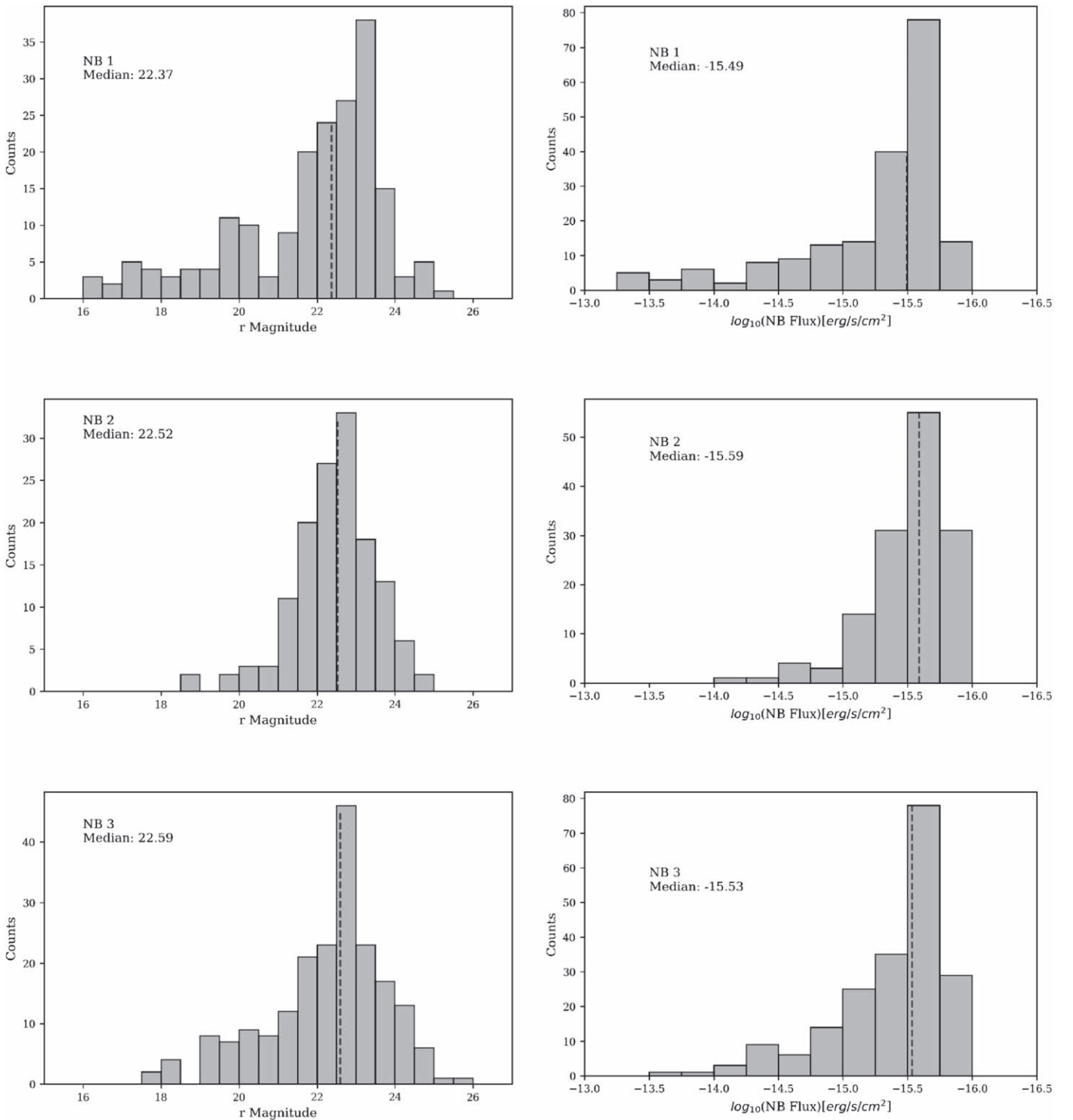


**Figure 8.** Distributions of  $r$ -band magnitude and NB flux broken down by NB filter. The left-hand plots show the  $r$ -band magnitude distributions for each of the pilot-study fields, while the right shows the NB flux distributions. From top to bottom is NB1, NB2, then NB3. The vertical dashed lines mark the median of each distribution. Again, there is a strong similarity between the distributions from the different filters, but with a few notable differences.

Figure 9 presents a plot of photometric error versus  $r$ -band magnitude for all 533 SFACT candidates. Out of the complete sample, 325 (61.0%) are detected in the SDSS database; these objects are plotted as blue dots, while the corresponding SDSS  $r$ -band photometry is plotted as gray dots. The remaining 208 SFACT objects (39.0%), plotted as red dots, are too faint to have been detected in SDSS. The differences in the error curves between SFACT and SDSS are expected, since SFACT is

carried out on a larger telescope and employs longer effective exposure times than SDSS.

The key point presented in Figure 9 is the high quality of the error curve for the SFACT photometry. The median value of  $\sigma_r$  for objects with  $r = 22.0 \pm 0.2$  is 0.061 mag. For SFACT sources with  $r \sim 23.0$  the median uncertainty is 0.104 mag, while at  $r \sim 24.0$  the median value of  $\sigma_r$  is 0.229 mag. The SFACT photometry yields high-integrity measurements well

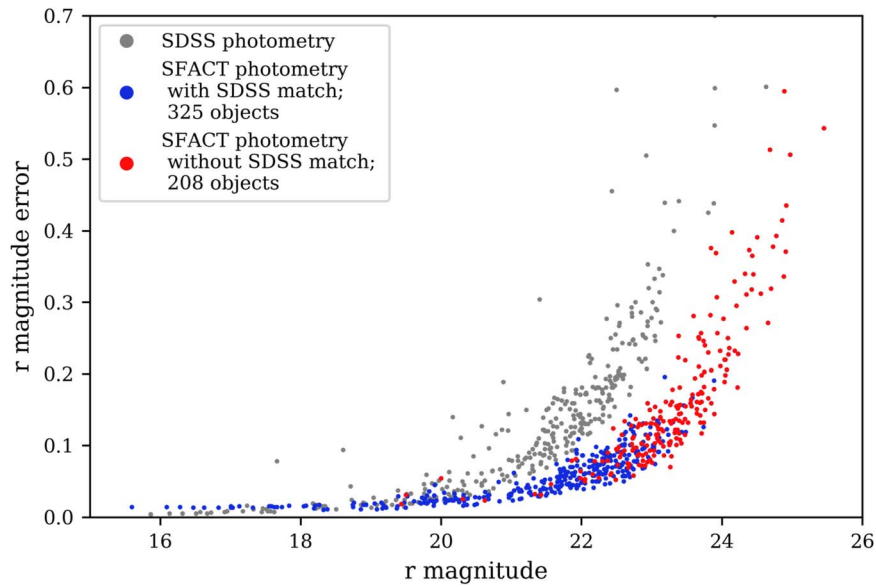


**Figure 9.** A plot of the photometric uncertainty vs.  $r$ -band magnitude for all 533 SFACT pilot-study objects. SFACT objects that are included in the SDSS catalog are shown in blue, while those that are not detected by SDSS are plotted in red. SDSS photometry for objects in common is shown in gray. The SFACT photometry is seen to have good fidelity to  $r \sim 24$ .

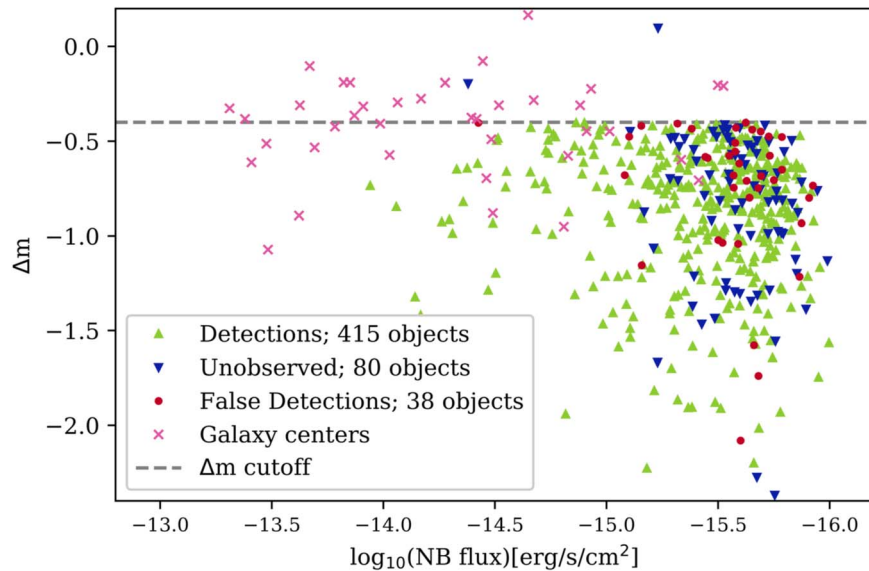


**Figure 10.** Shown here are the SFACT objects comparing their  $\Delta m$  against their measured NB flux. The dashed vertical line shows the cutoff of objects which proceed to the next step of the selection process. Objects marked as pink crosses are galaxy centers. Blue downward triangles are candidates that do not yet have follow-up spectroscopy. Green upward triangles have been confirmed as ELGs, and red circles denote objects which are confirmed to be false detections. The sample size of each is indicated in the legend.

beyond the median  $r$ -band magnitude of the sample (i.e.,  $r \sim 22.5$ ).

#### 4.4. Connecting Selection Parameters to Narrowband Flux

In this section, we investigate how well our measured emission-line fluxes correlate with the target-selection parameters we presented earlier in Figure 2. In Figure 10, we show the  $\Delta m$  values and the corresponding NB flux for each object. Because of our follow-up spectroscopy (discussed in SFACT3) we are able to denote confirmed emission-line objects (green upward triangles) and false detections (red circles) while also marking those which have yet to be observed (blue downward triangles). The dashed line marks the  $\Delta m$  cutoff of  $-0.4$  as one of our selection criteria to identify ELG candidates. Anything

above this line is a galaxy center (ExtG in Tables 2–4); these objects will always have an H II region located somewhere below the cutoff line.<sup>5</sup> There is no strong correlation between  $\Delta m$  and the strength of the emission line. This is expected since  $\Delta m$  is a flux ratio, which should not scale with an absolute flux.

Rather, we expect the strongest correlation to be between  $\Delta m$  and the emission-line EW. Since  $\Delta m$  is a measure of

<sup>5</sup> We note that, because of the way they are selected, our ExtG objects will not necessarily satisfy both of our selection criteria. The values of  $\Delta m$  and *ratio* for these objects are those associated with the galaxy center, which in some cases does not emit significant line flux. Hence, many of these sources will be located outside the ranges denoted by our selection limits in the plots shown in this section. These objects are valid SFACT objects since one or more H II regions found within the galaxy do satisfy our selection criteria.



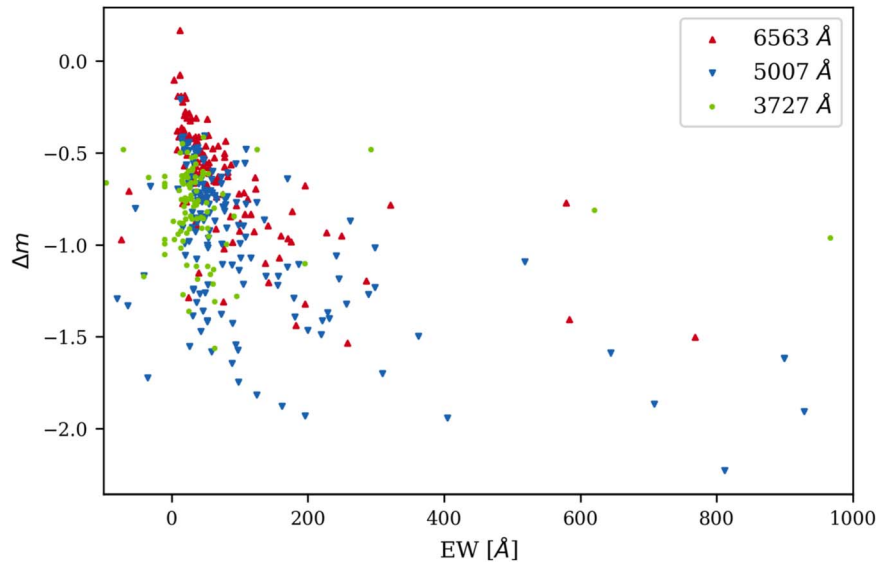


**Figure 11.** Shown here is the correlation between  $\Delta m$  and the emission-line equivalent widths (EWs) measured from our spectra (see SFACT3). Upward red triangles are objects detected via their  $H\alpha$  emission line, objects depicted as a blue downward triangle were detected via their  $[O III]$  emission line, and the green squares are all objects detected via their  $[O II]$  emission line. The spectroscopic EWs are highly uncertain, as explained in the text. Nevertheless, the expected trend of increasing EW with larger  $-\Delta m$  is visible.

excess flux in the difference image, we expect that a larger excess is driven by stronger line emission. However, as explained in SFACT3, our spectroscopic EW measurements are not all reliable. This is due to the sky-subtraction procedure followed for our multifiber spectra combined with the extremely faint nature of many of our objects. Our sky subtraction often oversubtracts the continuum by small amounts, leading to slightly negative continuum measurements for some of our faintest sources and resulting in indeterminate EWs. Even when the continuum is positive, this effect can result in unphysically large EWs (e.g.,  $EW_{5007} > 2000 \text{ \AA}$ ). While the majority of our spectroscopic EWs appear to be reliably measured, the outliers render our EWs dubious and undependable.

Despite this limitation, we can see the expected correlation between  $\Delta m$  and EW in Figure 11. There is a tendency for a larger  $-\Delta m$  to correlate with larger emission-line EW. This trend is true regardless of which emission line was detected in our NB filter. The figure indicates that there might be a tendency for the objects detected via  $\lambda 3727$  to have smaller EWs, but this could also be due to more distant and fainter objects having noisier spectra, and therefore a less well-determined continuum level. Further investigation will be conducted and addressed in future papers with a larger catalog.

Referring back to Figure 2, our object selection is based on both  $\Delta m$  and *ratio*. Hence, we next examine the relationship between the NB flux and the *ratio* parameter. Since *ratio* is a pseudo signal-to-noise measurement, a strong signal (larger flux) should translate to a higher value of *ratio*. We plot these two quantities in Figure 12. The upper plot shows the full range of values for these two parameters, and reveals a strong correlation. The only objects that deviate from the main trend are the ExtG objects, which is expected given the nature of these sources. The lower plot is zoomed in to smaller values of *ratio* in order to focus on the location of the majority of our objects. Most of the false detections are near the cutoff line, with 80% of the false detections below *ratio* = 8. Both plots

show a clear correlation between *ratio* and the measured NB flux, as expected.

## 5. Summary and Conclusions

We present the initial results of the SFACT NB emission-line survey. In the current paper, we have described in detail how the imaging portion of the survey is carried out, including our observational methodology, our data-processing procedures, and our object-selection method. We present our initial survey catalogs from the SFACT pilot-study fields, and present examples of detected ELGs.

By using the WIYN 3.5 m telescope and ODI camera, we make good use of the wide FOV to create science fields with robust image quality across the full field of the camera. WIYN also regularly achieves subarcsecond seeing and has an excellent light grasp, allowing us to detect faint objects. We create a stacked master image of the three custom NB filters and the three SDSS-like BB filters. This master image gives us the depth to detect very faint objects.

We detail the procedure used to discover potential ELGs in our NB images. We search for objects using the six-filter deep master image and then use preliminary photometry to identify those candidates that have an excess of NB flux. Our software detects candidates with significant excess flux in the NB images compared to the flux in the corresponding continuum image. These candidates are visually inspected in order to remove the image artifacts that have ELG-like signatures. Those remaining are considered SFACT candidates.

Aperture photometry is performed on all selected SFACT objects in both the BB and NB filters. SDSS stars in our images are used to calibrate the BB magnitudes, and spectrophotometric stars are used to put the NB fluxes on an appropriate NB flux scale. We also demonstrate that, due to the depth of our images and the resolution of our camera, we are able to achieve reliable photometry to fairly faint magnitudes.

The 533 SFACT sources and their properties are tabulated. In these three fields, we find a surface density of 355 emission-

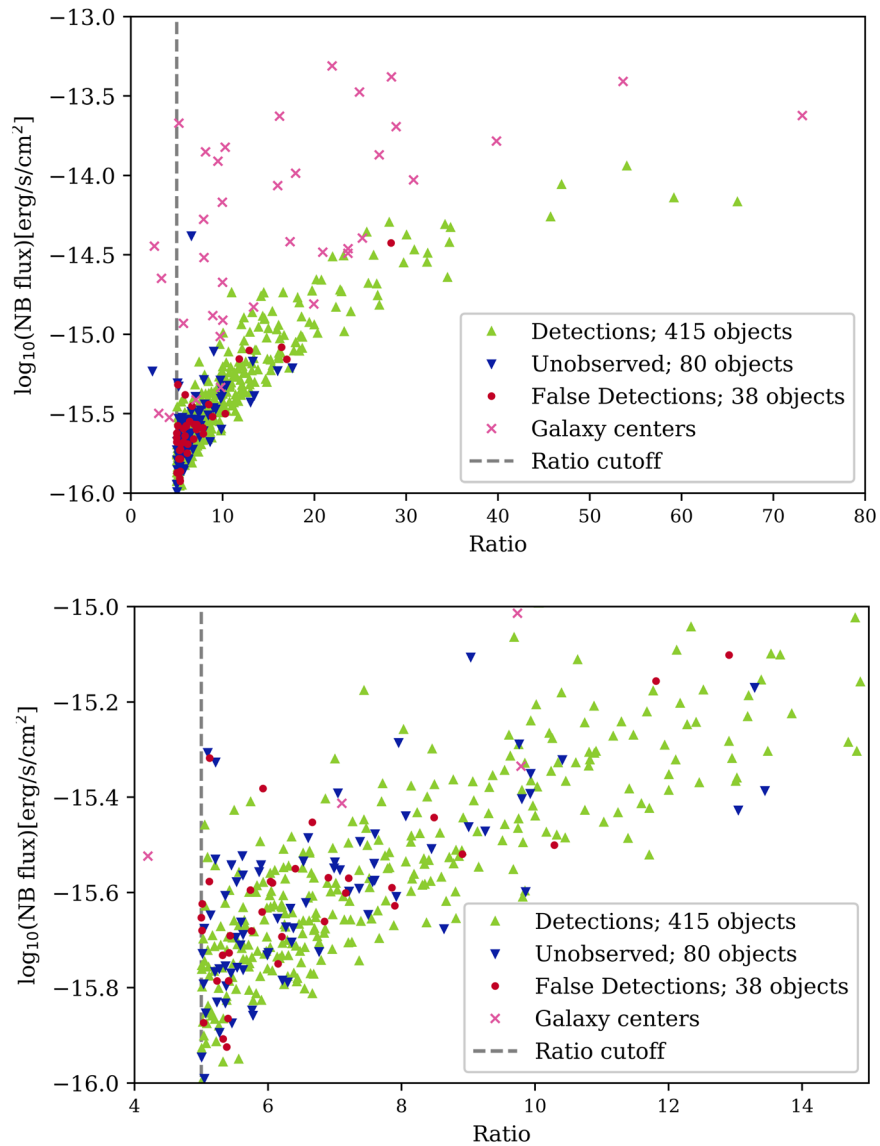


**Figure 12.** Shown here are the SFAC T objects comparing their *ratio* values against their measured NB flux. The dashed vertical line shows the cutoff of objects which proceed to the next step of filtering. Objects marked as pink crosses are galaxy centers. Blue downward triangles are candidates that do not yet have follow-up spectroscopy. Green upward triangles have been confirmed as ELGs, and red circles denote objects which are confirmed to be false detections. The sample size of each is indicated in the legend. The bottom plot is a zoomed in version focusing on the location of the false detections.

line objects  $\text{deg}^{-2}$ , offering significant improvement over previous emission-line surveys that also cover modest areas of the sky (i.e., tens of square degrees). Example candidates are shown for each of the primary emission lines ( $\text{H}\alpha$ ,  $[\text{O III}]\lambda 5007$ , and  $[\text{O II}]\lambda 3727$ ) as detected in each of our NB filters. We also present one QSO at  $z > 1$ , which was detected via its  $\text{C III}\lambda 1908$  line (SFF10-NB2-C21205 in Figure 6). These example images demonstrate the wide range of objects in the SFAC T catalog. Our study is dominated by faint compact objects such as SFF10-NB2-A8098, seen in Figure 5, yet SFAC T is also able to detect luminous QSOs. In the local Universe, SFAC T also detects numerous H II regions in large extended spirals like SFF15-NB1-A2606, seen in Figure 3.

The photometric and NB line flux levels found for our three survey fields also demonstrate stability and good agreement. We detect objects as faint as an *r*-band magnitude of 25 in each of our fields and, as Figures 7 and 8 demonstrate, this is achieved in all fields and in each filter. SFAC T is able to detect

objects with a wide range of properties all with robust photometry.

This paper focused on the photometric results of the SFAC T pilot-study fields. The corresponding spectroscopic confirmation results are discussed in greater detail in SFAC T3.

We currently have an additional 35 SFAC T survey fields processed, many of which already have partially complete spectroscopic follow-up observations. These fields have the benefit of improvements to the process based on this pilot study. With thousands of additional SFAC T objects in hand, future papers will begin to analyze global properties of the growing catalog and carry out the science applications planned for SFAC T, as detailed in SFAC T1.

### Acknowledgments

The authors are honored to be permitted to conduct astronomical research on Iolkam Du’ag (Kitt Peak), a mountain with particular significance to the Tohono O’odham.

The authors express their appreciation to the anonymous referee, who made a number of insightful suggestions that improved the quality of this paper.

We gratefully acknowledge the long-term financial support provided by the College of Arts and Sciences at Indiana University for the operation of the WIYN Observatory. Additional funds have been provided by the Department of Astronomy and the Office of the Vice Provost for Research at Indiana University to help support this project. The SFACT team wishes to thank the entire staff of the WIYN Observatory, whose dedication and hard work have made this survey possible. In particular, we acknowledge the contributions of Daniel Harbeck, Wilson Liu, Susan Ridgeway, and Jayadev Rajagopal. We also thank Ralf Kotulla (U. Wisconsin) for his development and continued support of the ODI image-processing software (QuickReduce), and Arvid Gopu and Michael Young (Indiana U) for their support of the ODI Pipeline, Portal & Archive. And we wish to thank the WIYN telescope operators without whom there would be no data. Finally, we acknowledge the contributions made at various stages of this project by students in the Department of Astronomy at Indiana University who assisted with the data processing: Bryce Cousins, Anjali Dziarski, Sean Strunk, and John Theising.

Funding for the SDSS and SDSS-II has been provided by the Alfred P. Sloan Foundation, the Participating Institutions, the National Science Foundation, the U.S. Department of Energy, the National Aeronautics and Space Administration, the Japanese Monbukagakusho, the Max Planck Society, and the Higher Education Funding Council for England. The SDSS website is <http://www.sdss.org/>.





The SDSS is managed by the Astrophysical Research Consortium for the Participating Institutions. The Participating Institutions are the American Museum of Natural History, Astrophysical Institute Potsdam, University of Basel, University of Cambridge, Case Western Reserve University, University of Chicago, Drexel University, Fermilab, the Institute for Advanced Study, the Japan Participation Group, Johns Hopkins University, the Joint Institute for Nuclear Astrophysics, the Kavli Institute for Particle Astrophysics and Cosmology, the Korean Scientist Group, the Chinese Academy of Sciences (LAMOST), Los Alamos National Laboratory, the Max-Planck-Institute for Astronomy (MPIA), the Max-Planck-Institute for Astrophysics (MPA), New Mexico State University, Ohio State University, University of Pittsburgh,

University of Portsmouth, Princeton University, the United States Naval Observatory, and the University of Washington.

*Facility:* WIYN:3.5 m.

*Software:* IRAF.

## ORCID iDs

Jennifer Sieben  <https://orcid.org/0000-0002-5513-4773>  
 David J. Carr  <https://orcid.org/0000-0002-4876-5382>  
 John J. Salzer  <https://orcid.org/0000-0001-8483-603X>  
 Alec S. Hirschauer  <https://orcid.org/0000-0002-2954-8622>

## References

- Aguado, D. S., Ahumada, R., Almeida, A., et al. 2019, *ApJS*, 240, 23  
 Bertin, E., Mellier, Y., Radovich, M., et al. 2002, *adass XI*, 281, 228  
 Boroson, T. A., Salzer, J. J., & Trotter, A. 1983, *ApJ*, 412, 524  
 Brunner, S. W., Salzer, J. J., Janowiecki, S., et al. 2020, *ApJ*, 898, 68  
 Cardamone, C., Schawinski, K., Sarzi, M., et al. 2009, *MNRAS*, 399, 1191  
 Carr, D. J., Sieben, J., Salzer, J. J., Brunner, S. W., & Cousins, B. 2023, *AJ*, 166, 102  
 Cook, D. O., Kasliwal, M. M., Van Sistine, A., et al. 2019, *ApJ*, 880, 7  
 Gaia Collaboration, Brown, A. G. A., Vallenari, A., et al. 2016a, *A&A*, 595, A2  
 Gaia Collaboration, Prusti, T., de Bruijne, J. H. J., et al. 2016b, *A&A*, 595, A1  
 Harbeck, D. R., Martin, P., Cavin, J., et al. 2010, *Proc. SPIE*, 7735, 77350G  
 Kakazu, Y., Cowie, L. L., & Hu, E. M. 2007, *ApJ*, 668, 853  
 Kellar, J. A., Salzer, J. J., Wegner, G., et al. 2012, *AJ*, 143, 145  
 Kennicutt, R. C., Lee, J. C., Funes, J. G., et al. 2008, *ApJS*, 178, 247  
 Khostovan, A. A., Malhotra, S., Rhoads, J. E., et al. 2020, *MNRAS*, 493, 3966  
 Kotulla, R. 2014, *adass XXIII*, 485, 375  
 Ly, C., Lee, J. C., Dale, D. A., et al. 2011, *ApJ*, 726, 109  
 MacAlpine, G. M., Smith, S. B., & Lewis, D. W. 1977, *ApJS*, 34, 95  
 Markarian, B. E., & Stepanian, D. A. 1983, *Afz*, 19, 639  
 Martínez-Solaesche, G., González Delgado, R. M., García-Benito, R., et al. 2022, *A&A*, 661, A99  
 Massey, P., Strobel, K., Barnes, J. V., et al. 1988, *ApJ*, 328, 315  
 Oke, J. B., & Gunn, J. E. 1983, *ApJ*, 266, 713  
 Ryan-Weber, E. V., Meurer, G. R., Freeman, K. C., et al. 2004, *AJ*, 127, 1431  
 Salzer, J. J., Carr, D. J., Sieben, J., Brunner, S. W., & Hirschauer, A. S. 2023, *AJ*, 166, 81  
 Salzer, J. J., Feddersen, J. R., Derloshon, K., et al. 2020, *AJ*, 160, 242  
 Salzer, J. J., Gronwall, C., Lipovetsky, V. A., et al. 2000, *AJ*, 120, 80  
 Sobral, D., Best, P. N., Matsuda, Y., et al. 2012, *MNRAS*, 420, 1926  
 Sobral, D., Smail, I., Best, P. N., et al. 2013, *MNRAS*, 428, 1128  
 Stetson, P. B. 1987, *PASP*, 99, 191  
 Stroe, A., & Sobral, D. 2015, *MNRAS*, 453, 242  
 Watkins, J. D., Salzer, J. J., Van Sistine, A., et al. 2021, *ApJS*, 253, 39  
 Werk, J. K., Putman, M. E., Meurer, G. R., et al. 2010, *AJ*, 139, 279  
 Yang, H., Malhotra, S., Gronke, M., et al. 2017, *ApJ*, 844, 171  
 York, D. G., Adelman, J., Anderson, J. E., et al. 2000, *AJ*, 120, 1579